atmosphere

MDPI

Article

Multi-Radar Analysis of the 20 May 2013 Moore, Oklahoma Supercell through Tornadogenesis and Intensification

Clarice N. Satrio [1,2,*], David J. Bodine [1,2], Robert D. Palmer [1,2] and Charles M. Kuster [3,4]

[1] Advanced Radar Research Center, University of Oklahoma, Norman, OK 73019, USA; bodine@ou.edu (D.J.B.); rpalmer@ou.edu (R.D.P.)
[2] School of Meteorology, University of Oklahoma, Norman, OK 73072, USA
[3] Cooperative Institute for Mesoscale Meteorological Studies, University of Oklahoma, Norman, OK 73072, USA; charles.kuster@noaa.gov
[4] NOAA/OAR National Severe Storms Laboratory, Norman, OK 73072, USA
* Correspondence: clarice.satrio@noaa.gov

Abstract: A multi-radar analysis of the 20 May 2013 Moore, Oklahoma, U.S. supercell is presented using three Weather Surveillance Radars 1988 Doppler (WSR-88Ds) and PX-1000, a rapid-scan, polarimetric, X-band radar, with a focus on the period between 1930 and 2008 UTC, encompassing supercell maturation through rapid tornado intensification. Owing to the 20-s temporal resolution of PX-1000, a detailed radar analysis of the hook echo is performed on (1) the microphysical characteristics through a hydrometeor classification algorithm (HCA)—inter-compared between X- and S-band for performance evaluation—including a hail and debris class and (2) kinematic properties of the low-level mesocyclone (LLM) assessed through ΔV_r analyses. Four transient intensifications in ΔV_r prior to tornadogenesis are documented and found to be associated with two prevalent internal rear-flank downdraft (RFD) momentum surges, the latter surge coincident with tornadogenesis. The momentum surges are marked by a rapidly advancing reflectivity (Z_H) gradient traversing around the LLM, descending reflectivity cores (DRCs), a drop in differential reflectivity (Z_{DR}) due to the advection of smaller drops into the hook echo, a decrease in correlation coefficient (ρ_{hv}), and the detection of debris from the HCA. Additionally, volumetric analyses of Z_{DR} and specific differential phase (K_{DP}) signatures show general diffusivity of the Z_{DR} arc even after tornadogenesis in contrast with explosive deepening of the K_{DP} foot downshear of the updraft. Similarly, while the vertical extent of the Z_{DR} and K_{DP} columns decrease leading up to tornadogenesis, the phasing of these signatures are offset after tornadogenesis, with the Z_{DR} column deepening the lagging of K_{DP}.

Keywords: supercell; polarimetric radar; tornado; differential reflectivity; specific differential phase; hydrometeor classification algorithm; internal rear-flank downdraft momentum surge

Citation: Satrio, C.N.; Bodine, D.J.; Palmer, R.D.; Kuster, C.M. Multi-Radar Analysis of the 20 May 2013 Moore, Oklahoma Supercell through Tornadogenesis and Intensification. *Atmosphere* **2021**, *12*, 313. https://doi.org/10.3390/atmos12030313

Academic Editor: Matthew Van Den Broeke

Received: 14 January 2021
Accepted: 24 February 2021
Published: 28 February 2021

1. Introduction

Characteristics of supercells and tornadoes are primarily analyzed through the use of radar observations and are greatly supplemented by the variety of sampling techniques utilized by each radar. The U.S. nationwide upgrade to polarimetric within the Weather Surveillance Radar 1988 Doppler (WSR-88D) radar network (completed in June 2013) brought widespread availability of polarimetric data to the the operational and research communities, which improved accuracy in depicting size, shape, and variety of hydrometeors and nonhydrometeors. Other recent advancements have focused on improving spatial and temporal sampling—bridging the gap between finescale processes (e.g., supercell and tornado evolution) and relatively slower temporal sampling of WSR-88Ds, whose timescales differ by 1–2 orders of magnitude—leading to the proliferation of mobile, rapid-scan, polarimetric radars in research (e.g., [1–3]). Such rapid-scan radars have the capability to observe the evolution of polarimetric signatures missed by operational radars, yet critical to understanding and predicting the formation and subsequent

behavior of severe hazards. The future of the operational radar networks in the U.S. and other countries is likely to incorporate such rapid-scan and dual-polarization capabilities into phased array radar systems [4–6]. In addition, rapid-scan radar systems are widely considered the future for meteorological research, owing to current limitations in temporal sampling capabilities [7].

One such region that has been extensively documented by WSR-88Ds and rapid-scan radars is the rear-flank downdraft (RFD), widely believed to be important to tornadogenesis processes. This has led to the identification of embedded regions of enhanced momentum and convergence within the broader-scale RFD, known as internal RFD momentum surges (the nomenclature associated with this feature varies within the literature and includes, but is not limited to, "secondary RFD surge/gust front", "RFD internal surge", and "embedded surge"), herein referred to as momentum surges. Radar observations of momentum surges, supplemented with in situ data [8–13] and numerical simulations [14–17], have shown that dynamic and thermodynamic properties within the momentum surge differ from that of the broader-scale RFD, implications of which are important in both tornadogenesis and dissipation processes. While studies have attempted to relate the aforementioned momentum surge characteristics to mesocyclone evolution [13,18–20], it remains unclear how momentum surges modify microphysical properties within the broader-scale RFD and hook echo and what role these microphysical changes might play in mesocyclogenesis/tornadogenesis.

Additional polarimetric signatures that provide insight into supercell and perhaps tornadogenesis processes include the differential reflectivity (Z_{DR}) arc, specific differential phase (K_{DP}) foot, Z_{DR} column, and K_{DP} column (e.g., [21–24]). Within the lowest 2 km, the Z_{DR} arc is a band of enhanced Z_{DR} located along the leading edge of the forward-flank downdraft (FFD) that develops as a result of drop size sorting (DSS) and size sorting of small hail [21,25,26]. Similarly, the K_{DP} foot is a region of enhanced K_{DP} located in the precipitation core of the FFD where liquid-water content (LWC) is relatively high [27]. The increased organization of both the Z_{DR} arc (increased curvature and magnitude; [28,29]) and K_{DP} foot (increased areal extent and a shift to downshear of the updraft; [29–31]) can be indicative of increasing likelihood of tornadogenesis.

Within the updraft, the perturbation of the 0 °C height upward by positively buoyant updraft air and delayed freezing of liquid hydrometeors results in higher concentrations of supercooled drops within the updraft and a small region of enhanced Z_{DR}, known as the Z_{DR} column (e.g., [21,32–41]). Similarly, the K_{DP} column is a region of enhanced K_{DP} above the ambient 0 °C height located adjacent to the Z_{DR} column (e.g., [27,37,38,40–43]), and is thought to be the result of the shedding of water drops from wet hailstone growth [42] and/or an abundance of mixed-phase hydrometeors [37], both of which lead to high LWC above the ambient 0 °C height. Thus, the presence of Z_{DR} and K_{DP} columns have been used to infer updraft characteristics, with deeper columns associated with stronger updrafts [39,41,44].

In addition to these Z_{DR} and K_{DP} signatures, ongoing severe weather hazards can be detected using polarimetric radars. Tornadoes can be remotely detected using the tornado debris signature (TDS; [45]), which is an area of reduced correlation coefficient (ρ_{hv}), near-zero Z_{DR}, and a wide range of reflectivity (Z_H; [46–50]). TDS parameters, such as TDS height, have shown a broad correlation to surface damage characteristics [47,51]. Moreover, TDSs appearing *prior* to tornadogenesis may provide information about a strengthening low-level mesocyclone (LLM) and impending tornadogenesis [23,52–54].

This study analyzes the 20 May 2013 tornadic supercell that produced a violent, long-track, EF5 tornado that tracked through central Oklahoma, leaving behind 24 fatalities and USD 2 billion in damages [12,55,56]. Previously, [56] documented debris ejections and rear-flank gust front surges, including a "failed occlusion" process, associated with the tornado using PX-1000, a mobile, rapid-scan, polarimetric, X-band radar that was situated south of the tornadic supercell at the University of Oklahoma's Westheimer Airport. Unlike [56],

however, this work will focus on the period prior to and through tornadogenesis/rapid intensification with the goal of:

1. Understanding the characteristics of debris lofting in a pre-tornadic mesocyclone and differences in debris detectability between radar wavelengths (S- and X-bands);
2. Exploring the structural evolution of the hook echo and associated changes in microphysical characteristics during momentum surges;
3. Examining how the characteristics of supercell polarimetric signatures relate to hail, DSS, and updrafts evolve through tornadogenesis and tornado intensification.

The study's goals are motivated by the need to improve tornado prediction and evolution, which required a better understanding of dynamic and microphysical processes in supercells observed by radar. A description of data and methods is provided in Section 2, followed by a discussion of the results in Section 3 and a summary of conclusions in Section 4. Within the results, findings from the hook echo and Z_{DR}/K_{DP} signature analyses are presented in Sections 3.1 and 3.2, respectively. Many of the analyses contained herein were done as part of the first author's MS thesis [57].

2. Data and Methods

2.1. Radar Specifications

The analysis of the 20 May 2013 supercell uses four radars that were operating in and around the Oklahoma City, Oklahoma, U.S. metropolitan area which captured the entirety of the supercell's life cycle (Figure 1). Namely, the supercell was observed by three operational and experimental WSR-88Ds—KTLX, KOUN, and KCRI—and the University of Oklahoma Advanced Radar Research Center's PX-1000, specifications of which are listed in Table 1. The WSR-88Ds have a narrower beamwidth than PX-1000 (1° compared to 1.8°) while PX-1000 provides finer range resolution (112 m oversampled to 30 m compared to 250 m). KTLX and KCRI collected data in a standard volume coverage pattern with 14 elevations spanning from 0.5° to 19.5°, resulting in a volume update rate of ∼4–5 min. On the other hand, KOUN operated in a rapid-scan, sectorized scanning strategy as part of National Severe Storms Laboratory's Rapid-Scan Polarization Experiment [58], with elevations from 0.5° to 10° and an update rate of ∼2–3 min. Lastly, PX-1000 was operating in a 2.6° single-elevation plan position indicator (PPI) scanning strategy with a 20-s update rate. Since PX-1000 operates using a pulse compression scheme [59], a time-frequency multiplexing method [60] is implemented to reconstruct the blind range (i.e., otherwise no returns can be measured within 10.3 km of the radar due to the use of pulse compression) while a multilag method ensures the accuracy and transition across the blind range [61]. Attenuation correction is applied to PX-1000 data using the $A_{H,DP} - K_{DP}$ parameterization method from [62], also described in [63]. A Z_{DR} calibration value of +0.4 dB for KTLX was determined using a reference dry snow value of +0.15 dB above the ambient melting height, similar to [45,53,64,65]—no calibration was determined to be necessary for KOUN and KCRI. PX-1000 data were calibrated using bird bath scans in 2013. To test the accuracy of polarimetric calibration, we compared KOUN and PX-1000 Z_{DR} in light to moderate rain and found the mean Z_{DR} to be within 0.1 dB. Although some uncertainty is noted in these comparisons due to attenuation at X-band, because PX-1000 did not scan above 2.4°, intercomparisons in areas of dry snow were not possible.

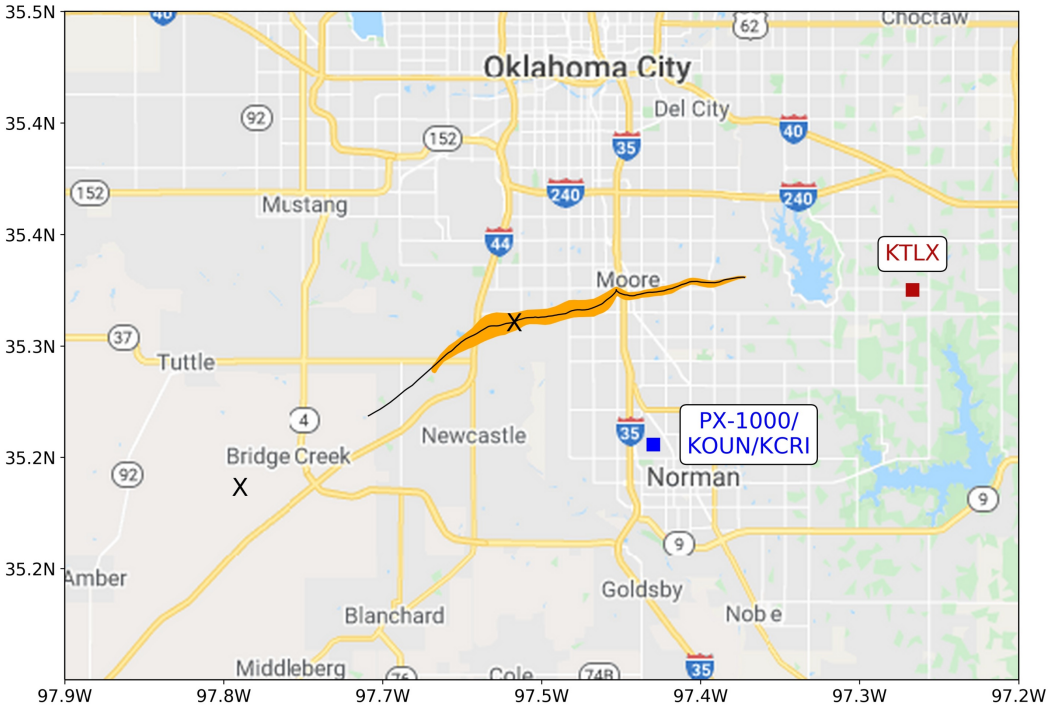

Figure 1. Map of the Oklahoma City, Oklahoma, U.S. metropolitan area overlaid with the National Weather Service Norman damage survey center track (black line) and EF-scale damage path (orange shading), with the "X"s denoting the start and end of the analysis period (1930–2008 UTC). The locations of the University of Oklahoma Advanced Radar Research Center's PX-1000 (Norman, Oklahoma, U.S.) and National Oceanic and Atmospheric Administration's (Norman, Oklahoma, U.S.) KOUN, and KCRI (blue square) and KTLX (red square) are plotted relative to the track.

Table 1. Radar and analysis specifications for PX-1000, KTLX, KOUN, and KCRI on 20 May 2013. The radar specifications consist of temporal, azimuthal, and range resolution, as well as beamwidth, and elevation angles. Asterisks denote the azimuthal resolution for the lowest three elevations; above the third elevation, azimuthal resolution is 1°. The analysis specifications consist of the respective analysis periods as well as beam height at and range to the low-level mesocyclone (LLM) for the lowest scanning elevation at the start of the analysis period/tornadogenesis (∼1956 UTC)/end of the analysis period.

	PX-1000	**KTLX**	**KOUN**	**KCRI**
Temporal Resolution	20 s	4–5 min	2–3 min	4–5 min
Azimuthal Resolution (°)	1	0.5 *	0.5 *	0.5 *
Beamwidth (°)	1.8	0.9	0.9	0.9
Range Resolution (m)	30	250	250	250
Elevation Angles (°)	2.6	0.5–19.5	0.5–10.0	0.5–19.5
Analysis Period (UTC)	1930–2008	1929–2008	1947–2007	1949–2008
Beam Height (km)	1.1/0.75/0.6	0.48/0.35/0.28	0.18/0.15/0.13	0.17/0.16/0.12
Range (km)	24.3/16.3/13.1	42.6/32.8/27.2	18.7/15.9/13.6	17.8/16.4/13.1

With the exception of Doppler velocity (V_r), all data used in the analysis were converted to a regular Cartesian grid. Note that V_r was not interpolated to a regular grid to avoid over-averaging, and was dealiased using standard unfolding techniques via Solo II, a software program developed by the National Center for Atmospheric Research to display radar sweeps and allow the user to manually edit fields. In this case, areas where V_r is aliased/folded were identified and dealiased/unfolded based on the Nyquist velocity. PX-1000 data are linearly interpolated to a 0.1 km × 0.1 km horizontal grid while volumetric data from the WSR-88Ds are interpolated to a 3D 0.25 km × 0.25 km × 0.25 km

grid. Although the generation and amplification of small-scale noise as a result of a linear interpolation scheme is possible [66] (p. 288), [67] found linear interpolation to perform better than [68,69] schemes in terms of root-mean-square error. Prior to 3D interpolation, volumetric data collected by the WSR-88Ds are converted in space-time to account for storm motion to ensure vertical continuity. Storm motion between two subsequent volumetric scans is calculated using subjectively chosen center points at each time that represent the center of the LLM.

2.2. Hydrometeor Classification Algorithm

The HCA implemented in this study is based on a fuzzy logic approach which utilizes membership functions and decision criteria that accounts for measurement error, beam broadening effects, melting layer, and precipitation type [45,70,71]. For S-band, [71] defines 10 classifiers: (1) ground clutter (GC)/anomalous propogation, (2) biological scatterers, (3) dry snow, (4) wet snow, (5) crystals, (6) graupel, (7) big drops (BD), (8) rain (RA), (9) heavy rain (HR), and (10) rain/hail (RH; cf. Table 1 in [71]); however, biological scatterers and all frozen precipitation classes except hail (2–6) are omitted to further restrict classes. The five remaining classifiers are extended to X-band except that the HCA values for X-band are adapted from [63] which better captures Mie scattering regimes, given in Table 2—note that the Z_H and Z_{DR} membership functions from [63] are modified slightly for RA, HR, and RH to ensure that RA is representative of smaller drops (decrease in upper range of Z_H) and RH is hail-only (increase in lower range of Z_H).

Table 2. Hydrometeor classification algorithm (HCA) membership functions and weights for ground clutter (GC), big drops (BD), rain (RA), heavy rain (HR), and rain/hail (RH) classes for X-band adapted from [63] with bolded numbers highlighting modified values—A_1 and A_2 are two-dimensional functions of Z_H as in [63]. S-band functions for the aforementioned classes are not listed but are given in [71]. Membership functions and weights for the small hail (SH), large hail (LH), and giant hail (GH) classes are adapted from [72] while tornado debris signature (TDS) membership values are from [49]; values for these four classes are implemented for both X- and S-band.

	GC	**BD**	**RA**	**HR**	**RH**	**SH**	**LH**	**GH**	**TDS**
					Z_H (dBZ)				
x_1	15	24	5	**40**	**45**	45	54	54	30
x_2	20	29	10	47	**55**	49	59	64	35
x_3	70	49	**37**	57	65	59	64	74	70
x_4	80	54	**42**	62	**75**	64	69	80	75
					Z_{DR} (dB)				
x_1	-4	$A_2 - 0.6$	$\mathbf{A_1 - 5}$	$\mathbf{A_1 - 5}$	$\mathbf{A_1 - 5}$	1	0.4	0	-2.5
x_2	-2	$A_2 - 0.3$	A_1	A_1	$\mathbf{A_1}$	1.5	0.9	0.5	-1.5
x_3	1	A_3	A_2	A_2	$\mathbf{A_2}$	2.5	1.9	1.5	1.5
x_4	2	$A_2 + 1$	$A_2 + 0.5$	$A_2 + 0.5$	$\mathbf{A_2 + 0.5}$	4	3.5	2	2.5
					ρ_{hv}				
x_1	0.5	0.92	0.95	0.92	0.80	0.94	0.88	0.8	0
x_2	0.6	0.93	0.96	0.94	0.85	0.96	0.92	0.88	0.01
x_3	0.9	1	1	1	0.95	0.98	0.98	0.96	0.85
x_4	0.95	1.01	1.01	1.01	1.01	0.99	0.99	0.98	0.92
					Weights				
Z_H	0.2	0.8	1	1	1	1	1	1	0.6
Z_{DR}	0.4	1	0.8	0.8	0.8	0.8	0.8	0.8	0.8
ρ_{hv}	1	0.6	0.6	0.6	0.6	0.6	0.6	0.6	1

The RH class for both X- and S-band has been expanded to include small hail (SH, $D < 2.5$ cm), large hail (LH, $2.5 < D < 5$ cm), and giant hail (GH, $D > 5$ cm; adapted from [72]). Membership functions for the different hail classes are the same across X- and S-band, but could be modified in future studies based on scattering or observational data. A final modification to the HCA includes the addition of a TDS class. Membership functions for TDS are given in the last column of Table 2, based on values from [49], and are implemented for both X- and S-band—a grid point must also have ρ_{hv} less than 0.92, Z_H greater than 25 dBZ, and be within 3 km of the LLM in order to be classified as a TDS point. For ease of reference, the HCA classifiers presented in this study are listed in Table 3 with their associated abbreviations.

Table 3. List of HCA abbreviations and respective classifiers.

Abbreviation	Classifier
GC	Ground Clutter/Anomalous Propagation
BD	Big Drops
RA	Rain
HR	Heavy Rain
RH	Rain/Hail
SH	Small Hail
LH	Large Hail
GH	Giant Hail
TDS	Tornado Debris Signature

2.3. Z_{DR} and K_{DP} Detection

As a result of uncertainty with attenuation correction at X-band, the Z_{DR} arc and K_{DP} foot analysis relies on KTLX and KOUN for consistency in interpreting results. Additionally, the use of KTLX and KOUN allows for analysis of 3D characteristics of these signatures, with deeper areas representative of more mature regions of the Z_{DR} arc and K_{DP} foot. The data were restricted through a subjective mask outlining the supercell, along with additional constraints of Z_H greater than 30 dBZ and ρ_{hv} greater than 0.85, such that no external influences bias the results (e.g., storm mergers and noisy data). Lastly, data are restricted to below 2 km since the Z_{DR} arc and K_{DP} foot are typically found below this altitude [21,73].

In order for a grid point to be defined as "enhanced", Z_{DR} (K_{DP}) must exceed 3.5 dB (1.5° km^{-1}); these thresholds are consistent with [74] and are used for both KTLX and KOUN. For each horizontal grid point, the number of vertical grid points below 2 km above ground level (AGL) for which Z_{DR} and K_{DP} is enhanced is multiplied by the vertical resolution (0.25 km) to calculate the depth of the Z_{DR} arc and K_{DP} foot (hereafter referred to as the depth field). The depth field is then smoothed using a Gaussian filter with a standard deviation of 0.5 km. From the depth field, the total volumetric extent of the Z_{DR} arc and K_{DP} foot is calculated by

$$\Delta_{xy}^2 \sum_{i,j} D_{ij} \quad (1)$$

where Δ_{xy} is the horizontal grid spacing, in this case 0.25 km, and D_{ij} is the depth of the field at the i, jth grid point.

The depth field for the Z_{DR} and K_{DP} column analysis is calculated similar to the Z_{DR} arc and K_{DP} foot. However, because these features should be collocated with or in close proximity to the updraft, the data are restricted to within 5 km of the LLM. The Z_{DR} and K_{DP} columns are restricted to above 4.2 km, which represents the ambient melting height as per the 1800 UTC Norman, Oklahoma sounding (not shown). In order to be considered enhanced, Z_{DR} and K_{DP} must exceed 2.0 dB and 1.0° km^{-1}, respectively. Trends in the Z_{DR} and K_{DP} columns were found to be insensitive to choice of threshold value, e.g., 1.0 dB as used in [44] for Z_{DR} column. Because the focus of this study is on trends rather than specific

magnitudes of depth/volumetric extent, the results are not dependent on the selection of threshold values.

Linear interpolation of data and HCA calculations were conducted using MATLAB while all other analyses and figure generation were done in Python.

3. Results

Conditions on this day were favorable for supercells and tornadoes, with convective initiation focused along an eastward bulge in the north-south oriented dryline in southwestern Oklahoma (see [56] for further details on synoptic conditions). By 1930 UTC, the storm exhibited supercellular characteristics with a large precipitation core in the forward-flank region and a relatively wide hook echo appendage. The supercell rapidly organized in the next 15 min, particularly with regard to the hook echo, which was characterized by a narrowing extension of higher Z_H into the hook echo. By 1955:06 UTC (formatted HHMM:SS), precipitation surrounding the LLM became increasingly heavy and was coincident with the interaction of two echo mergers: (1) a supercell to the north of the primary supercell and (2) remnants of a cell to the south which directly interacted with the parent supercell inflow region (hereafter referred to as the echo merger). Of importance is an east–west oriented boundary (distinguishable through KTLX, Figure 2) which is collocated with the hook echo after the supercell deviates to the right. The supercell persisted on the boundary through at least the duration of the analysis period (through 2008 UTC). The influence of the boundary can be seen with a convective flanking line extending westward from the hook echo region in Figure 3, especially at 1935:12 and 1940:11 UTC. The boundary may have provided enhanced pre-existing vorticity resulting in favorable conditions for tornadogenesis, which occurred at ∼1956 UTC [as concluded by National Weather Service Norman], and maintenance [75–78]. To our knowledge, previous studies documenting this case have not mentioned the presence of this boundary. Whereas future investigation into the origin and characteristics of this boundary should be undertaken, it is speculated that this boundary is a stationary remnant outflow boundary from convection the day prior.

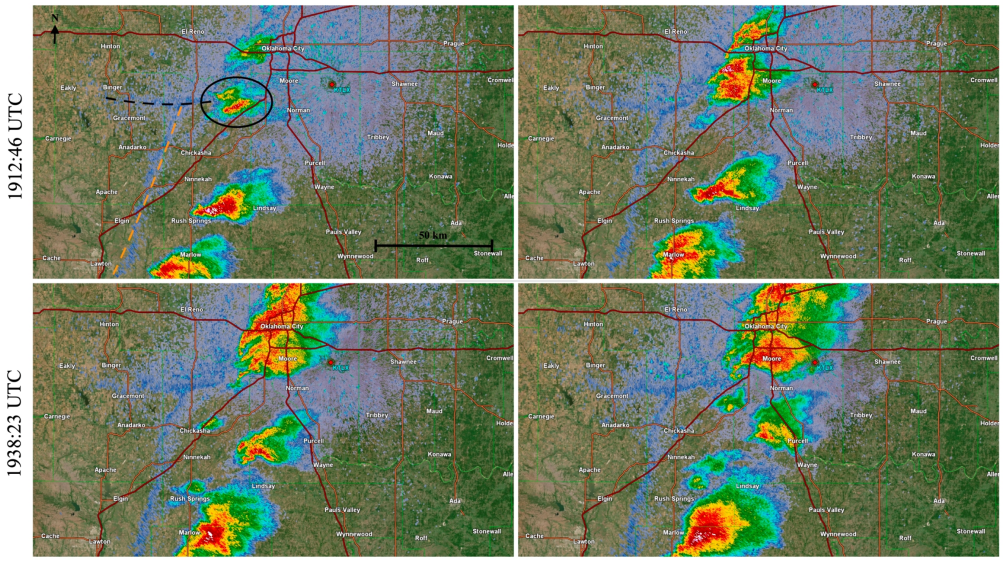

Figure 2. Sequential evolution of reflectivity (Z_H) as observed by KTLX at 0.5°, highlighting the interaction of the Moore supercell (circled in first panel) with the dryline (dashed orange) and east–west oriented boundary (dashed black). Time is formatted HHMM:SS. Images created from GR2Analyst software.

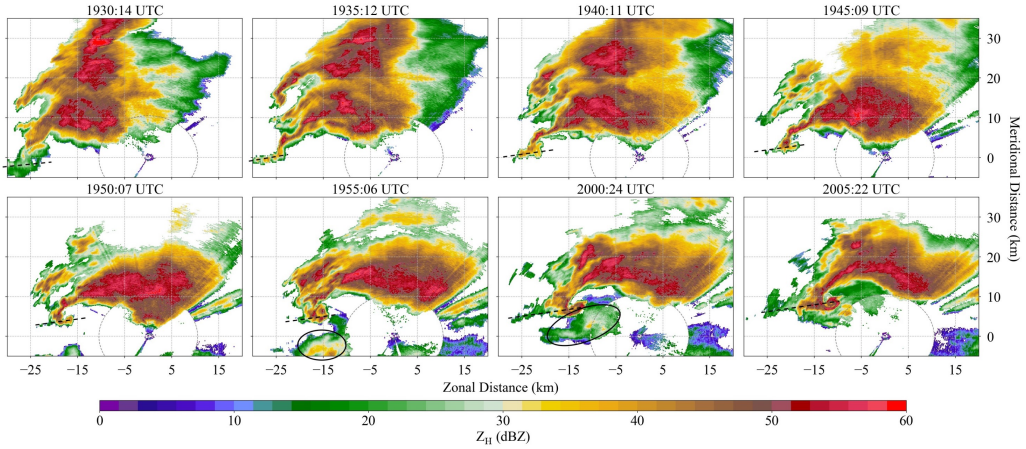

Figure 3. Radar scans of Z_H from PX-1000 every ∼5 min from 1930:14 to 2005:22 UTC showing the overall evolution of the supercell during the majority of the analysis period. The dashed gray circle denotes the blind range at 10.3 km range from the radar. Influence of precipitation entrainment within the inflow region is denoted with solid black ovals while the boundary is marked by the dashed black line. The zonal and meridional distances are relative to radar location.

3.1. Microphysical Properties and Characteristics within the Hook Echo

3.1.1. Evolution of the Low-Level Mesocyclone and Tornado

To understand how tornadogenesis and tornado intensification relate to storm processes, an objective method is employed to quantify tornado vortex signature strength by taking the difference between local maxima in inbound and outbound V_r (hereafter ΔV_r). Quantification of ΔV_r highlights the necessity of rapid-scan radar in detecting finer-scale trends which WSR-88D cannot temporally resolve. Moreover, trends in microphysical characteristics presented herein are related back to LLM strength deduced from ΔV_r. The ΔV_r calculations for each elevation are range-restricted to within 2 km of the LLM to mitigate the sampling of winds not associated with the LLM. Additionally, ΔV_r analyses were only applied to PX-1000, KCRI, and KOUN since these radars are nearly-collocated, avoiding any discrepancies with KTLX due to the offset in position (e.g., spatial resolution).

In the period prior to tornadogenesis, there are no consistent patterns in ΔV_r, with the exception of slight strengthening above 3 km per KCRI from ∼1949 to ∼1953 UTC (Figure 4). Regardless, nearly all ΔV_r for all heights and times from 1930–2008 UTC consistently exceeds 40 m s^{-1}, which corresponds to higher-end criteria differentiating tornadic circulations from nontornadic [79–82]. The strongest ΔV_r below 1 km prior to tornadogenesis occurs with transient intensifications detected through the 20-s PX-1000 ΔV_r analysis. Three distinct, prolonged transient intensifications occur at ∼1943, ∼1947, and ∼1949 UTC and last ∼1–2 min (see ovals in Figure 4); a shorter intensification also occurs at ∼1952 UTC. Past studies have noted such periodicities in ΔV_r associated with tornadoes (primarily strong and violent ones) as well as with the mesocyclone aloft [81,83]. The periodicities in this case may be associated with mesocyclone-scale processes, such as momentum surges, discussed in further detail in Section 3.1.3. Nonetheless, ΔV_r suggests that there is a strong, transient rotation near the ground preceding tornadogenesis with additional evidence provided through TDS quantification, discussed in Section 3.1.2.

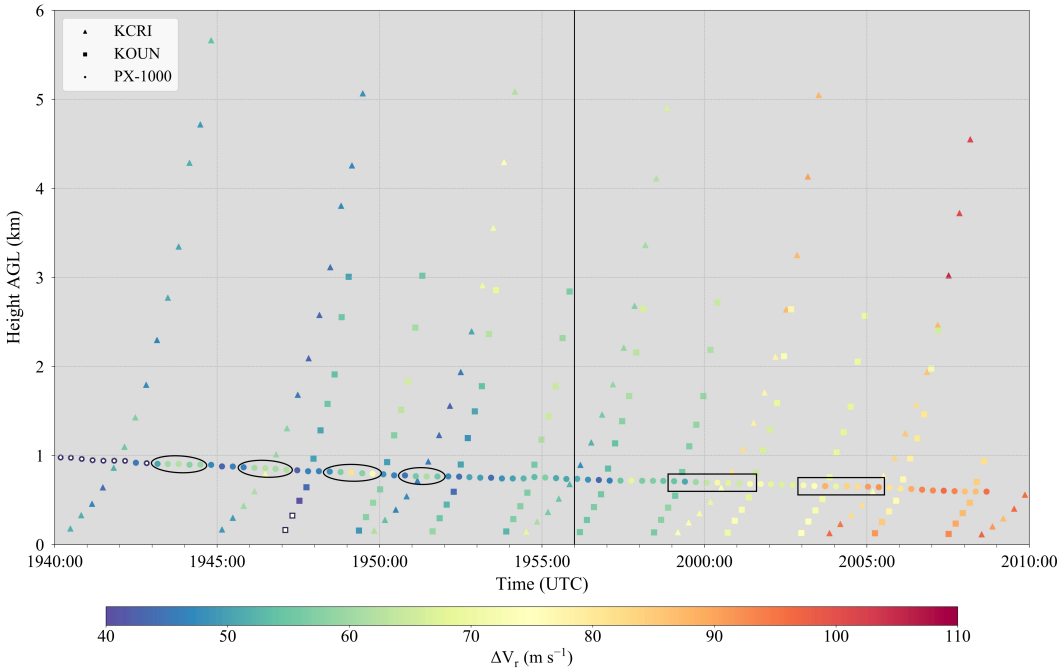

Figure 4. Time series of time-height corrected ΔV_r plotted above ground level (AGL) for PX-1000 (circles), KCRI (triangles), and KOUN (squares). The color bar comprises the spectrum of tornadic intensity seen on 20 May 2013, with subtornadic intensity (ΔV_r below 40 m s^{-1}) depicted as white markers outlined in black. The solid black vertical line denotes the time of tornadogenesis at ∼1956 UTC. The solid black ovals prior to tornadogenesis mark the four periods of transient intensifications of the low-level mesocyclone (LLM), as captured by PX-1000, while the solid black rectangles after tornadogenesis signify the two periods of rapid intensification.

There is a lack of a substantial trends in ΔV_r in the period corresponding to, and just after, tornadogenesis. As per PX-1000, it is not until 1959–2001 UTC, 3–5 min after tornadogenesis, in which the first period of rapid intensification from ∼50 m s^{-1} to ∼70–80 m s^{-1} occurs. There is a subsequent period of no substantial trend in ΔV_r from ∼2001 to ∼2004 UTC, followed by a secondary period of rapid intensification to greater than 90 m s^{-1}. KCRI and KOUN also indicate that in the minutes prior to tornadogenesis, ΔV_r strengthening is mainly restricted to regions higher than 1 km AGL. It is not until the first period of rapid intensification (∼1959 UTC) in which there is significant strengthening in ΔV_r below 1 km AGL, though even at this point, ΔV_r further aloft (above 3 km AGL) still remains stronger than below 1 km AGL per KCRI. Similar to PX-1000, KCRI and KOUN observe a secondary strengthening of ΔV_r to greater than 90 m s^{-1} at ∼2004 UTC, after which ΔV_r at the lowest altitudes (<0.5 km AGL) exceed that in the mid-altitudes (0.5–3 km AGL), with KCRI showing a successive increase to stronger ΔV_r values above 3 km.

3.1.2. Multi-Wavelength Comparison of HCA for Hydrometeors and Debris

Multi-wavelength comparisons of polarimetric signatures in supercells are rare, and have not yet been conducted for TDSs at X- and S-bands. Intercomparisons between X- and S-band performance are valuable as (1) transmit frequencies of operational radars around the world are diverse [84], including X- and S-bands presented here, and (2) future gap-filling radar networks in the U.S. may operate at X-band [85]. Using the HCA (Section 2.2), intercomparisons are done with single elevation scans from PX-1000, KCRI, and KOUN, which are collocated and scanning at single elevation angles (2.6, 2.4, and 3.0°, respectively). This comparative analysis assumes the S-band radars as "truth", since they are less susceptible to attenuation and can serve as a reliable evaluation of the performance for the X-band HCA.

The HCA time series indicate that X- and S-band HCAs exhibit respectable agreement with each other for hail and TDS classes (Figure 5b,c, respectively). However, greater

differences are seen between the rain classifications at S- and X-bands with a larger areal extent of BD (RA) at S- (X-) bands, respectively. This is likely due to residual errors after attenuation correction (e.g., due to substantial hail). Because the analysis herein focuses on the evolution of TDS within the hook echo, *compared* to rain classifications for a single radar, rather than the differences within the rain classifications among multiple radars, this discrepancy is not detrimental to the results of this study. Nevertheless, future work should include testing differing values of the HCA ranges and coefficients given in Table 2 to minimize the discrepancies between X- and S-band rain classifications.

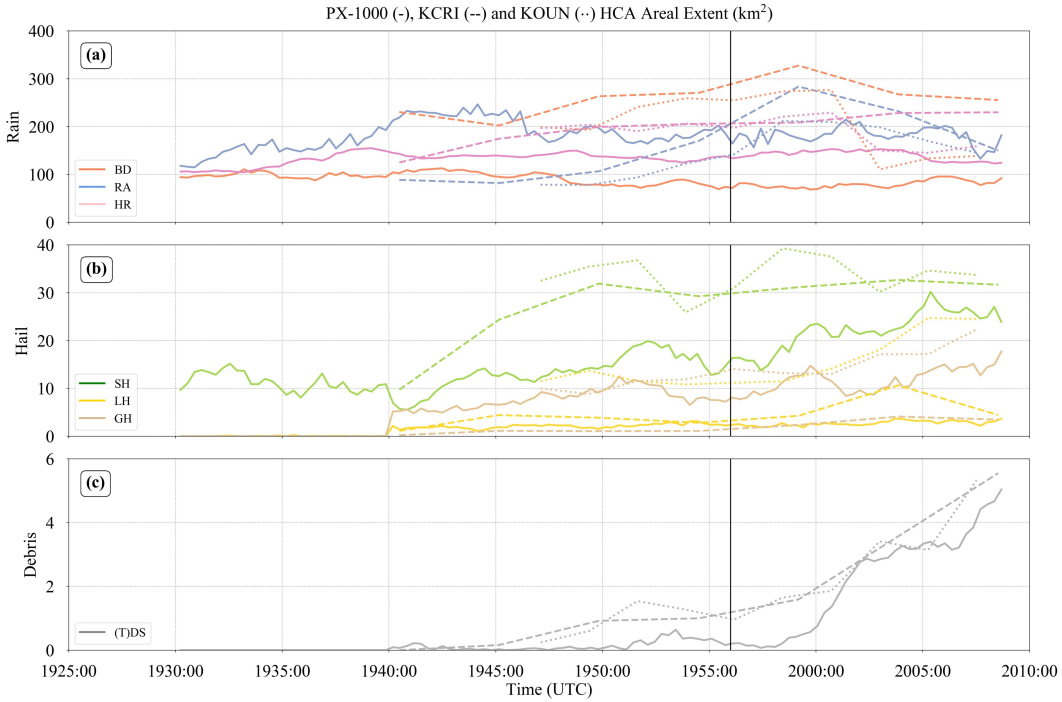

Figure 5. Time series in HCA areal extent for (**a**) rain (BD, RA, and HR), (**b**) hail (SH, LH, and GH), and (**c**) debris ((T)DS) classes for PX-1000 (solid line), KCRI (dashed line), and KOUN (dotted line). The elevations for KCRI (2.4°) and KOUN (3.0°) are chosen to be closest in beam height to PX-1000 (2.6°). The solid black vertical line denotes the time of tornadogenesis at ∼1956 UTC.

Hail classifications on the other hand (SH, LH, and GH) show agreement between X- and S-bands in the slow but steady increasing trend of all three classes (Figure 5b). However, the HCA tends to produce smaller areas of all hail classes at X-band compared to S-band, particularly for SH. Since SH is associated with positive Z_{DR}, differential attenuation may be a contributing factor (e.g., residual errors in correction from rain-hail volumes). Moreover, non-Rayleigh effects from larger hail may result in low ρ_{hv}, which may explain why there is a greater discrepancy between SH compared to the larger hail classes. It is also notable that the area of GH for PX-1000 is much larger than the area of LH. Further investigation reveals that differential attenuation results in negative or near-zero Z_{DR} regions along the northern edge of the precipitation core—since near-zero Z_{DR} is a large driver in GH detection, the HCA algorithm for PX-1000 tends to overestimate the GH class. Due to this performance issue, any analysis that utilizes HCA hail classes will not rely on PX-1000; modifying the membership functions for hail to alleviate this issue is beyond the scope of this study and is left for future work.

There is a high degree of consistency in both the trend and areal extent within the pattern for TDS detection among all radars (Figure 5c), suggesting that the S-band membership functions for TDS, defined in [49], also perform well for X-band. TDS quantification is less subject to attenuation since the radar beam passes through a relatively short path with heavy precipitation/hail (in contrast to the FFD region). On the same note, however,

because of the higher sensitivity of X-band to raindrops compared to debris, the detection of the TDS by ρ_{hv} is affected more significantly by precipitation entrainment than at S-band [86]. Moreover, Z_H may be larger at S-band compared to X-band, enhancing the likelihood of being classified as TDS. Therefore, KCRI and KOUN consistently detect a higher areal extent of TDS through much of the period, particularly prior to tornadogenesis when less debris is present and precipitation is more likely to be the dominant scatterer type, i.e., when precipitation entrainment from the echo merger is considerable. While PX-1000 steadily decreases to near-zero TDS at ∼1958 UTC, KCRI and KOUN continue detecting 1–2 km^2 of TDS, though it still decreases in area by about 30% due to the echo merger. Following the first period of rapid ΔV_r intensification from 1959 to 2003 UTC and attendant increase in along-track damage [12], the more significant lofting of debris dominates precipitation entrainment effects, and the PX-1000 areal extent in TDS closely resembles that of KCRI and KOUN. While differences between S- and X-band debris detectability have been hypothesized, until now they have not been examined with observational comparisons [86]. Despite the reduction in TDS detectability using X-band during heavy precipitation entrainment or reduced debris lofting periods, the consistency of the trend in TDS areal extent between PX-1000 and KCRI/KOUN demonstrates the successful implementation of TDS detection across X- and S-band radar wavelengths for tornadoes lofting large amounts of debris.

The high sensitivity and rapid-scan capabilities of PX-1000 sufficiently capture debris lofting patterns in a pre-tornadic mesocyclone, evident through TDS quantification. Hereafter, to differentiate between an HCA TDS before and after tornadogenesis, detected TDS occurring prior to 1956 UTC will be referred to as a debris signature (DS) and those occurring after will be referred to as a TDS; this is in an attempt to clarify that TDS detected before tornadogenesis are not necessarily detecting tornadic debris, but rather lofted non-meteorological scatterers in general, while still maintaining consistency with nomenclature in [49]. The earliest detection of a DS occurs at ∼1942 UTC, 14 min prior to tornadogenesis, and was also noted in [52] with KTLX. Overall, T(DS) is detected 60% of the time between 1930 and 2008 UTC with 56% DS detection prior to tornadogenesis; however, the detection of DS is sporadic and only becomes more persistent as it transitions to a TDS. The intermittency of DS corresponds to the periodicities seen in ΔV_r, with increases in DS areal extent occurring during periods of higher ΔV_r, e.g., at ∼1952 UTC. Moreover, since ΔV_r often exceeded the criteria of a tornadic circulation, the presence of a strong LLM with brief intensifications may have contributed to the formation of periodic DSs, which are found to be associated with three distinct momentum surges.

3.1.3. Evolution of Momentum Surges

Past studies have noted that precipitation in the hook echo, enhanced through processes such as descending reflectivity cores (DRCs), may intensify convergence and instigate tornadogenesis [87]—the momentum surges seen prior to tornadogenesis include both DRCs as well as rapid enhancement and advection of precipitation within the hook echo. The supercell produced two salient momentum surges captured by PX-1000 at 1952:27 and 1957:05 UTC (hereafter surge A and B corresponding to Figures 6 and 7, respectively). Note that the times of each surge correspond peak maturity, objectively defined as the time the surge apex position is furthest ahead of the LLM (relative to storm motion). Momentum surges are identified through strengthening V_r (inbound relative to PX-1000) surging ahead of the LLM, manifested as aforementioned transient intensifications in ΔV_r, and are marked by the detection of DS and a sharp Z_H gradient on the outflow side of the LLM, which traverses around cyclonically, resulting in heavier precipitation surrounding the LLM.

The RFD region is associated with variable and unique drop size distributions (DSDs) with smaller drops concentrating on the outer periphery of the hook echo (cf. Figure 10 in [88]). The author in [88] hypothesized that the spatial inhomogeneity of DSDs within the hook echo is the result of (1) concentration of larger drops along the inflow side of the hook echo, owing to the extension of the Z_{DR} arc towards the LLM and (2) dynamically-induced

downdrafts transporting smaller drops from aloft down to the surface along the outflow side of the hook echo, though the exact process by which smaller drops concentrate on the periphery of the hook echo is beyond the scope of this study. Thus, momentum surges can transport smaller drops from the outer periphery closer to the LLM, resulting in reduced Z_{DR} around the LLM. The following section documents the changes in hook echo structure and microphysical composition during both momentum surges, along with its role in the detection of sporadic DS and relation to tornadogenesis processes.

Surges A and B progress in a similar manner, with the surge traversing cyclonically around the LLM over a period of ~4–5 min with stronger inbound V_r surging out ahead of the LLM (Figures 6b and 7b). A characteristic feature of these surges is a Z_H gradient that traverses cyclonically around the LLM, resulting in overall higher Z_H around the LLM by the peak of the surge (Figures 6a and 7a)—the wrapping Z_H gradient is better shown at 20-s temporal resolution in Figures 8 and 9. Rough calculations from Figures 8 and 9 reveal that the apex of the Z_H gradient, as well as pockets of high Z_H behind the leading gradient in surge B, are translating at 25–30 m s^{-1} and accelerate as these features approach the LLM. Since hook echoes are critically important to studies of tornadoes, there are two additional features resolved by the high-temporal resolution of PX-1000 that are worth noting that relate to structural evolution of the hook echo. First, both surges feature precipitation filaments on the outer edge of the hook echo that advect cyclonically around the LLM; though these precipitation filaments may be a result of hydrometeor ejection, further investigation is necessary to conclusively determine their origin. Second, as the Z_H gradient and associated pockets advect cyclonically around the LLM, a tertiary pocket of high Z_H appears at 1955:06 and 1955:26 UTC, suggestive of a DRC occurring just before tornadogenesis (Figure 9d–f). The DRC remains relatively stationary in a storm-relative sense, which may reflect the descent of precipitation as opposed to rapid horizontally advected precipitation associated with a momentum surge.

For surge A, advection of smaller drops into the hook echo leads to both a subsequent decrease in Z_{DR} (Figure 6c) and an increase in RA (Figure 6e) by surge maturation at 1952:27 UTC. This process is obscured in surge B, as heavier precipitation entrainment masks the influence of small drop advection and is instead characterized by a dominance of HR within the hook echo (Figure 7e; HR being indicative of drops of larger size and concentration comparative to RA). Surge A occurs in conjunction with the lofting of small nonmeteorological scatterers, which lowers ρ_{hv} within the hook echo (Figure 6d) and contributes to the detection of DS (Figure 6e). While the onset of surge B is also marked by DS, precipitation entrainment from the echo merger and adjacent DRC leads to an increase in ρ_{hv} (Figure 7d) and thus, the replacement of DS by HR by 1957:05 UTC (Figure 7e).

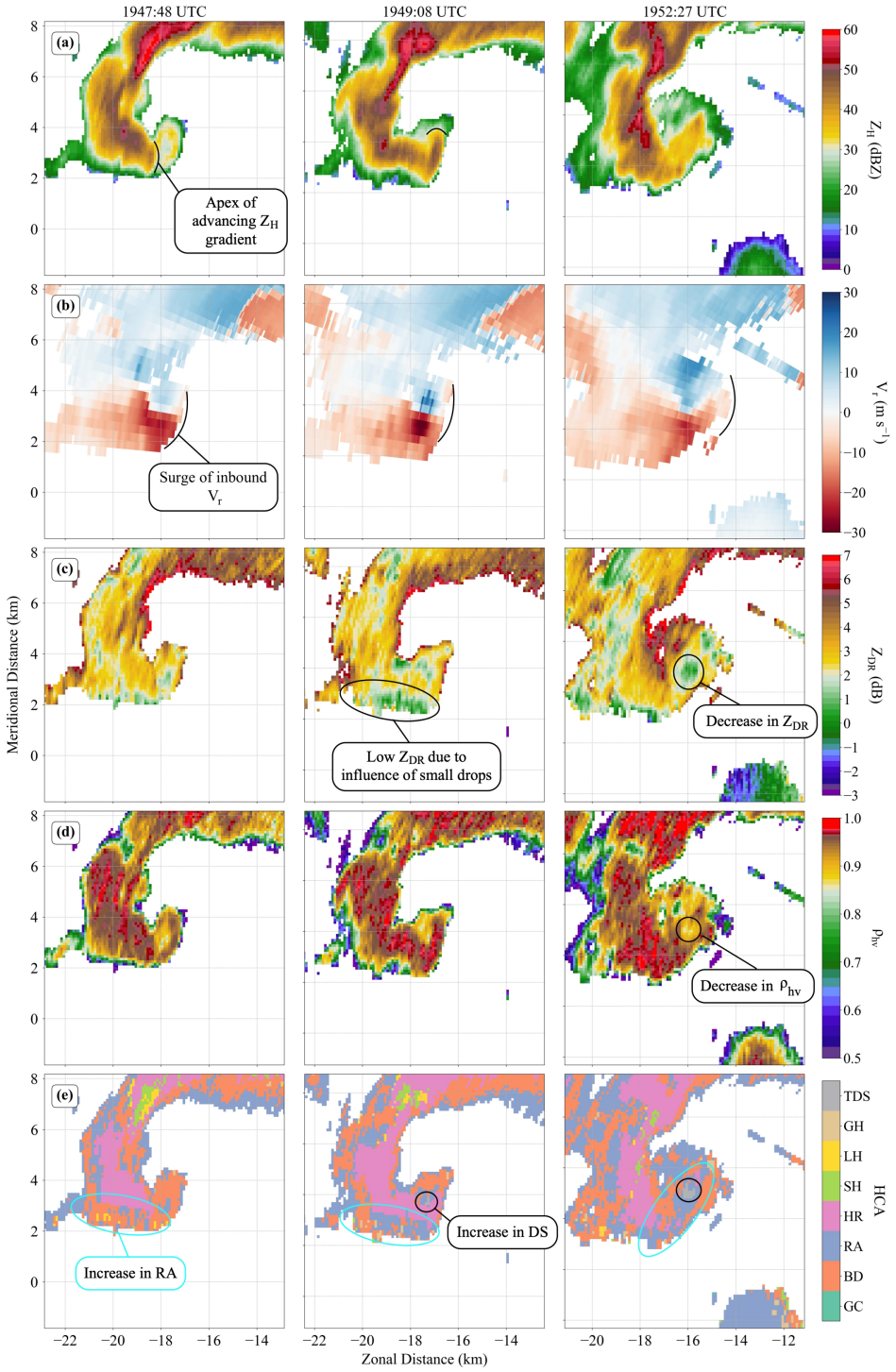

Figure 6. From top to bottom row (**a**–**e**): Z_H, Doppler velocity (V_r), differential reflectivity (Z_{DR}), correlation coefficient (ρ_{hv}), and HCA from PX-1000 for three subsequent times—from the left to right column, 1947:48, 1949:08, and 1952:27 UTC—highlighting surge A. Annotations detail polarimetric characteristics associated with the evolution of the momentum surge.

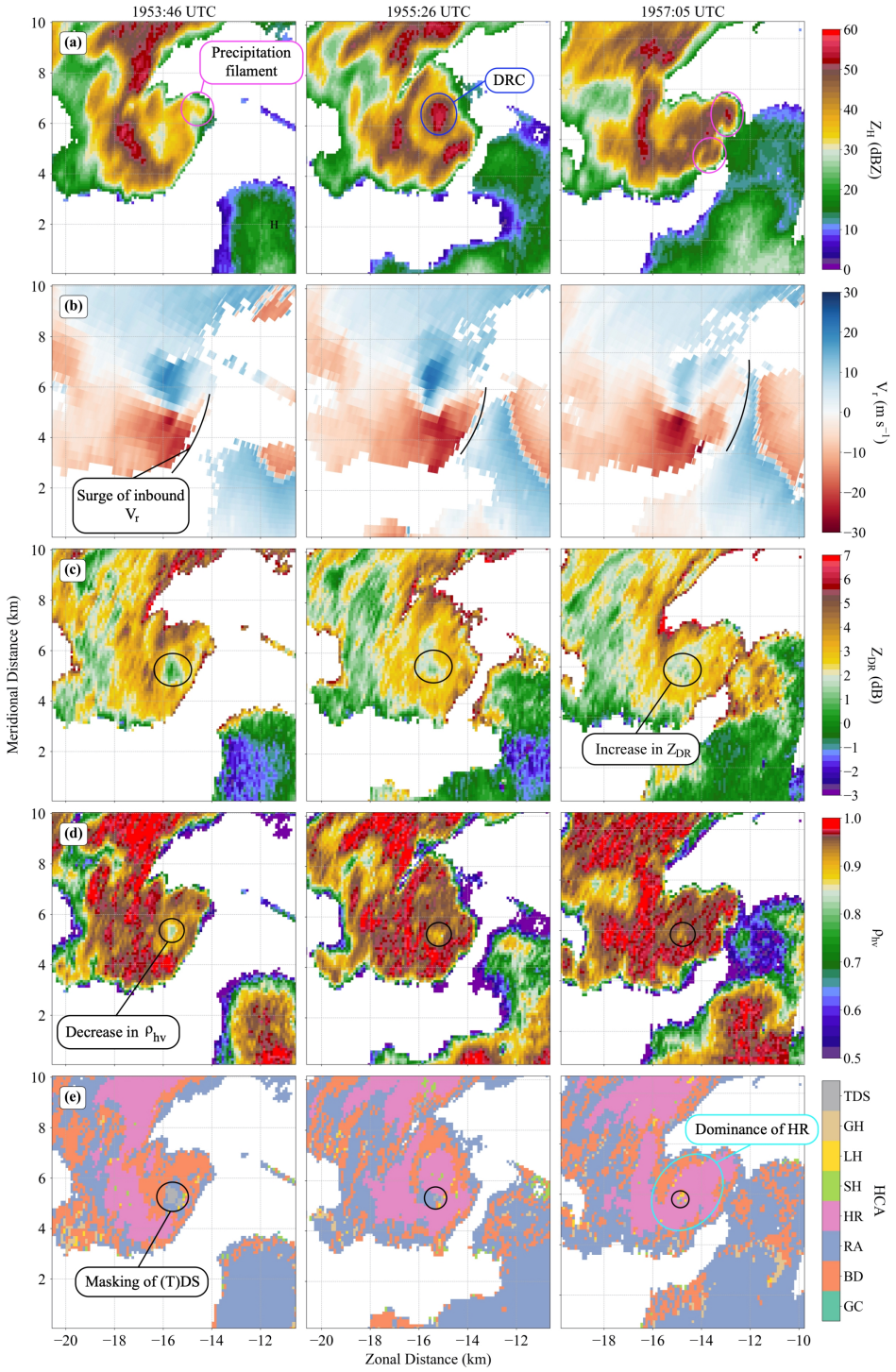

Figure 7. From top to bottom row (**a**–**e**): Z_H, Doppler velocity (V_r), differential reflectivity (Z_{DR}), correlation coefficient (ρ_{hv}), and HCA from PX-1000 for three subsequent times—from the left to right column, 1947:48, 1949:08, and 1952:27 UTC—highlighting surge A. Annotations detail polarimetric characteristics associated with the evolution of the momentum surge, except for surge B at 1953:46, 1955:26, and 1957:05 UTC.

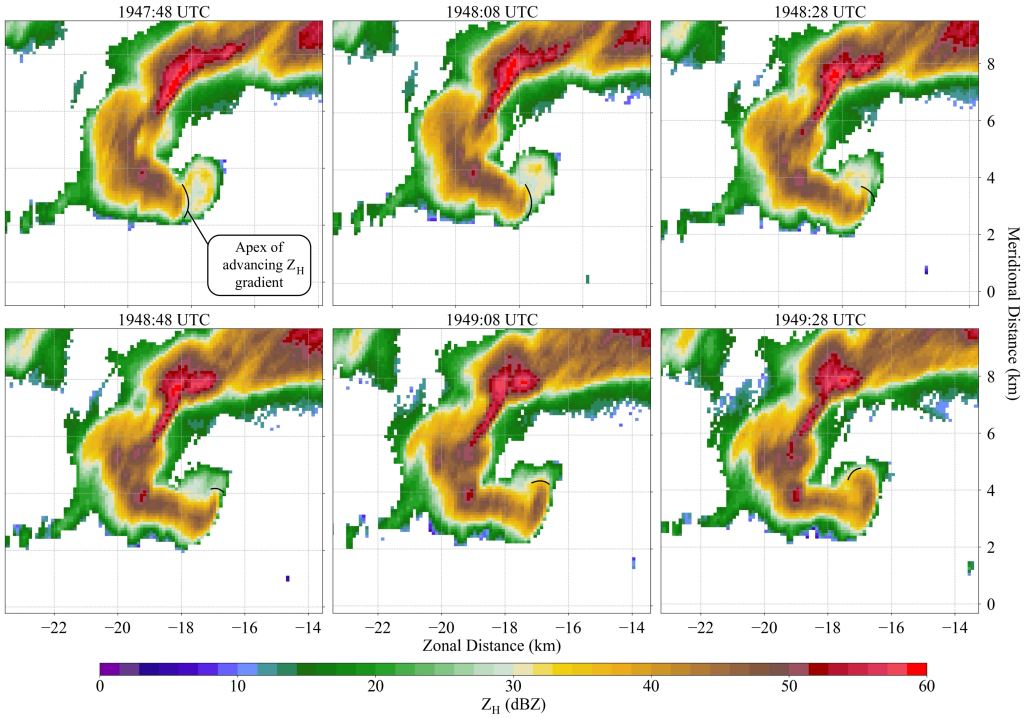

Figure 8. Six consecutive radar scans from PX-1000 of Z_H every 20 s from 1947:48 to 1949:28 UTC highlighting the advancing Z_H gradient during surge A.

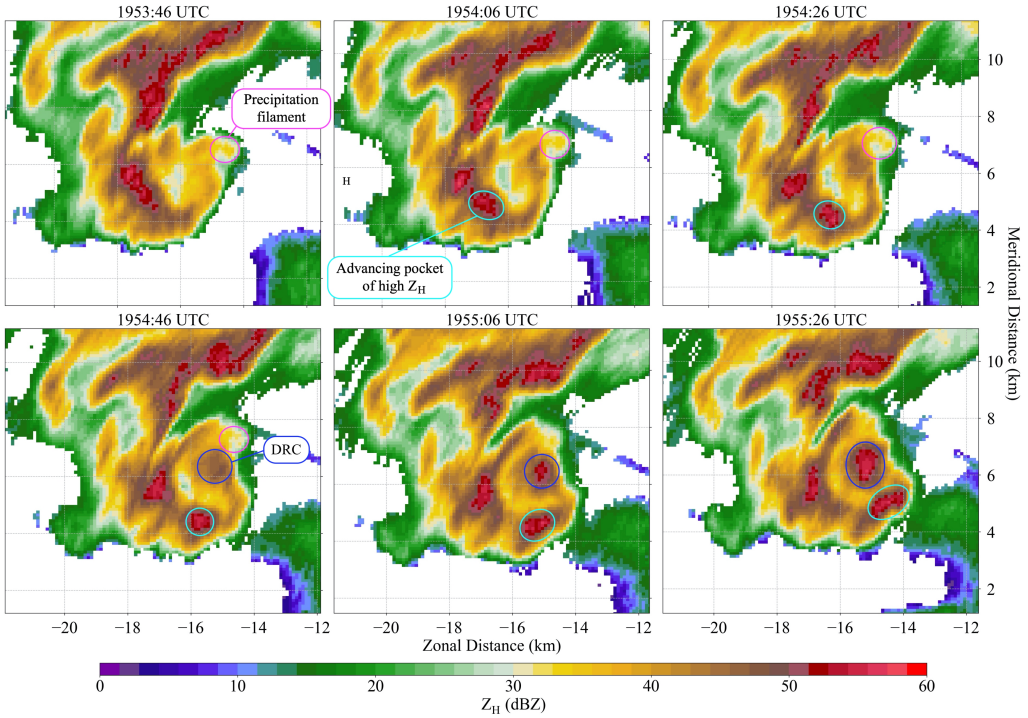

Figure 9. As in Figure 8, except from 1953:46 to 1955:26 UTC, highlighting the advancing Z_H gradient during surge B.

In both surges, as the Z_H gradient is advected cyclonically around the hook echo, there is a transient increase in ΔV_r at ~1949 and ~1952 UTC, respectively, exceeding the criteria for tornadic circulation, but this is not sustained. The authors in [55] also noted an

increase in ΔV_r just prior to 1953 UTC (surge B) that coincided with confluent damage/tree fall patterns analyzed using high-resolution satellite imagery, which may be suggestive of a weak, short-lived tornado [89]; these findings were further supported by video evidence of a brief debris cloud near the ground. In combination, the strong transient intensification of ΔV_r (over 80 m s^{-1}), the presence of DS, and a relatively dense area of damage indicators associated with surge B, it is possible that a brief tornado may have occurred, but ultimately failed to sustain itself. This mode of tornadogenesis would be consistent with [87], who found that rain curtains—manifested as both rapid cyclonic advection of hydrometeors as well as the DRC at ~1955 UTC—can instigate tornadogenesis through enhanced convergence and downward transport of angular momentum. Transport of higher angular momentum downward and into the LLM by the DRC can play a significant role in LLM strength and tornadogenesis/maintenance [79,80], and can tilt baroclinically-generated vortex lines generating near-surface vertical vorticity [79,80,90–92]. Numerical simulations from [92–95] also found that a strong LLM at ~1 km AGL plays an essential role in tornadogenesis by enhancing upward acceleration and convergence near the ground. However, as a result of inconclusive evidence of earlier tornado formation from damage surveys, the official time of tornadogenesis was determined to occur at ~1956 UTC.

To quantitatively explore the variability of the microphysical composition of the hook echo during the momentum surges, the time series of median Z_{DR} and ρ_{hv} as well as the area of BD, RA, and (T)DS within 2 km of the LLM are examined in Figure 10a,b, respectively. Median calculations are intended to eliminate the influence of outliers and are further restricted to grid points with Z_H and ρ_{hv} greater than 20 dBZ and 0.7, respectively, to ensure erroneous data do not affect the trends. Trends in Z_{DR} and ρ_{hv} are relatively consistent until ~1942 UTC, at which point both median Z_{DR} and ρ_{hv} begin to decrease (Figure 10a). Z_{DR} trends downward until ~1952 UTC, likely owing to (1) concentration of small drops along the outflow-side periphery of the hook echo and (2) transportation of small drops toward the LLM by surges A and B. These processes are supported by a decrease in BD and increase in RA over the same time period (Figure 10b). However, the consistent decreasing trend in median Z_{DR} makes it difficult to distinguish deviations away from the overall trend directly owing to surges A and B. On the other hand, median ρ_{hv} undergoes two periods of subsequent decrease and increase, resulting in two local minima—one at ~1946 UTC (median ρ_{hv} = 0.92) and the sharper, second minimum at ~1952 UTC (median ρ_{hv} = 0.9), which are a direct result of possible lofted nonmeteorological scatterers from surge A and the onset of surge B. The latter is nearly simultaneous with a sharp increase in DS, maximizing at 1953–1954 UTC, followed by an abrupt decrease immediately after due to the precipitation entrainment at 1957:05 UTC. Thus, tornadogenesis is marked by median ρ_{hv} greater than 0.95 and the detection of only a few (albeit nonzero) TDS. Through the exploration of the hook echo in a high temporal observational framework, the role momentum surges play in changing the structural and microphysical composition of the hook echo, and how these processes may impact mesocyclogenesis/tornadogenesis, is better understood.

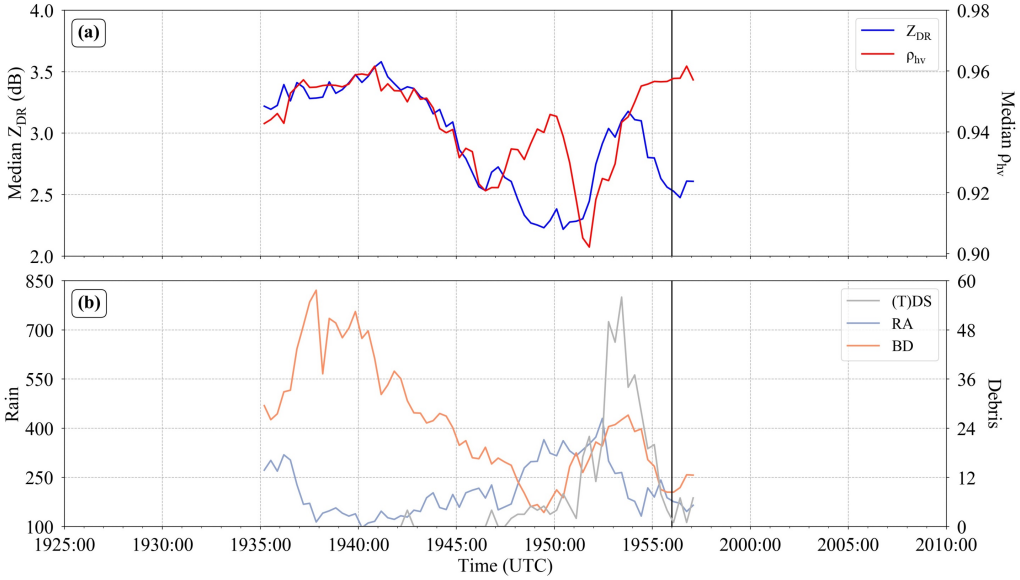

Figure 10. Using PX-1000: (**a**) Time series of the median Z_{DR} and ρ_{hv} within the hook echo from 1935 to 1957 UTC and (**b**) count of interpolated grid points where the HCA detects (T)DS (gray), RA (blue), and BD (orange). The solid black vertical line in both subfigures denotes the time of tornadogenesis.

3.2. Z_{DR} and K_{DP} Signatures

While past studies have suggested that polarimetric signatures of supercells may help distinguish between tornadic and nontornadic storms [29,31,96], few studies have considered the evolution of multiple signatures with high-temporal resolution V_r. Volumetric properties of the Z_{DR} arc/K_{DP} foot and Z_{DR}/K_{DP} columns are used to investigate how their characteristics relate to hail, DSS, and updrafts, and how they evolve through tornadogenesis and tornado intensification. Moreover, this study aims to fill a gap in the exploration of K_{DP} signatures, which has not been examined as closely as Z_{DR}—in addition, a volumetric quantification and direct comparisons between the two, as presented here, are scarce. Unlike Section 3.1, which relied heavily on PX-1000, Z_{DR} and K_{DP} analysis depends on S-band, particularly that of KTLX split into two periods: the first from 1929:49–1946:55 UTC and the second from 1951:11–2008:11 UTC.

3.2.1. Z_{DR} Arc and K_{DP} Foot

Owing to attenuation uncertainties within the FFD and more importantly, limitation to single-elevation PPIs of PX-1000, the analysis relies on KTLX and KOUN—higher-temporal sampling of KOUN is used only to verify patterns found in KTLX since KOUN data are limited to 1947–2007 UTC. Figure 11 illustrates that patterns in both Z_{DR} arc and K_{DP} foot volume and depth found with KOUN are indeed consistent with KTLX; thus, temporal sampling from KTLX is sufficiently capturing longer temporal trends in the Z_{DR} arc and K_{DP} foot.

Though both the Z_{DR} arc and K_{DP} foot show an increase in volumetric extent during the first period from 1929:49–1946:55 UTC (Figure 11a), the depth of the K_{DP} foot deepens from approximately 0.75 km at 1929:49 UTC to 1.3 km by 1946:55 UTC, whereas the depth of the Z_{DR} arc remains relatively steady at around 1.0 km (Figure 11b). This pattern is indicative of the Z_{DR} arc becoming more diffuse through the first period. Figure 12 confirms these patterns—while areal extent of Z_{DR} arc and K_{DP} foot increase during the first period to encompass the majority of the FFD, only the K_{DP} foot steadily deepens during the latter half of this time period. The relative shallowness of the Z_{DR} arc compared to the K_{DP} foot suggests that, while DSS processes for larger drops are occurring in a relatively shallow layer, small and medium drops are concentrating within a deeper layer downshear of the updraft. This finding is consistent with [29,30] which have noted consolidation of the K_{DP} foot downshear of the updraft preceding tornadogenesis, although the former analyzed

only the horizontal extent of the K_{DP} foot and the latter analyzed only nonsupercellular tornadic storms.

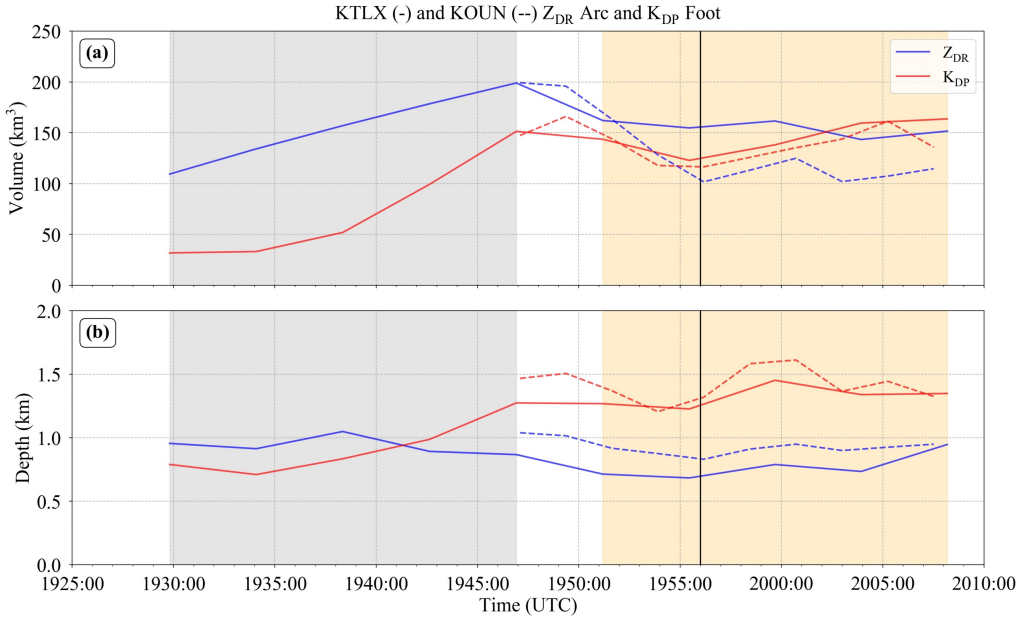

Figure 11. Using KTLX (solid lines) and KOUN (dashed lines): Time series of Z_{DR} arc and specific differential phase (K_{DP}) foot (**a**) volumetric extent of the enhancement regions and (**b**) 90th percentile of the depth of the enhancement regions. The gray and orange shaded regions mark the first and second period, respectively, with the solid black vertical line denoting the time of tornadogenesis.

In this case, the shedding of excess water from hailstones surrounded by a liquid-water torus into small and medium drops is hypothesized to be partially responsible for the consolidation of the K_{DP} foot, especially from 1938:21 to 1946:55 UTC. Evidence of this is provided per the quantification of HCA hail from KTLX, with a substantial shift in the height distribution of hail to lower elevations during the first period (Figure 13); for example, the bulk of the distribution of giant hail shifts from above 6 km to at or below 2 km. The most rapid shift in the distribution, indicating when hail fallout is most prevalent, is coincident with the deepening of the K_{DP} foot, suggesting that either water shedding and/or melting of small hail and increased precipitation production in the FFD is contributing to the increase in LWC downshear of the updraft. Such a sharp gradient of LWC suggests the potential for baroclinic vorticity generation with greater evaporative cooling and melting potential associated with high LWC in the northern part of the FFD, as opposed to larger drops to the south with less evaporative cooling potential—however, thermodynamic observations would be needed to confirm this.

The second period from 1951:11 to 2008:11 UTC is characterized by a relative steadiness in both the volumetric extent and depth of the Z_{DR} arc and K_{DP} foot (Figure 11)—the magnitudes of any fluctuations are small relative to the rapid growth of the K_{DP} foot in the first period. The K_{DP} foot remains deeper and larger in volumetric extent than the Z_{DR} arc, still a result of small and medium drops concentrating within a deep high LWC layer downshear of the updraft. Lower elevations still contain the bulk of the hail distributions (Figure 13), suggesting the continuation of water shedding contributing to a high LWC. The K_{DP} foot remains visually mature, with a clear maximum in the depth field within the FFD while the Z_{DR} arc exhibits increasing diffuseness, especially at 1955:27 UTC, and no sizeable consolidation and deepening until 2008:11 UTC (Figure 14). While studies such as [28,29] noted a maturation of the Z_{DR} arc leading up to tornadogenesis, the diffuseness of the Z_{DR} arc in conjunction with high hail concentrations below 2 km is consistent with [28,64,73,97], which found that hail can disrupt DSS processes and, by extension, the Z_{DR} arc.

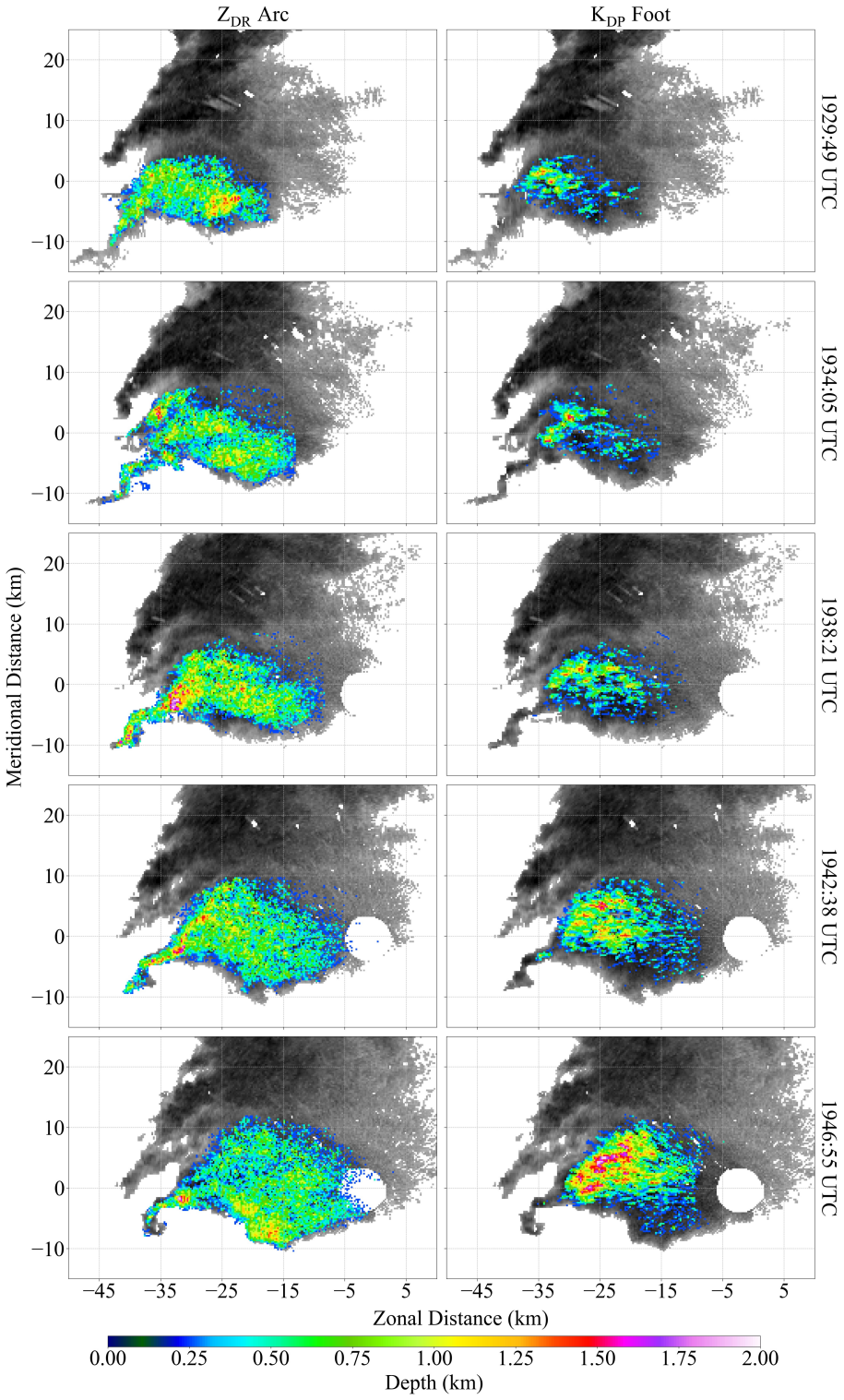

Figure 12. Plot of the depth field for Z_{DR} arc and K_{DP} foot from KTLX for five consecutive radar scans from 1929:49 to 1946:55 UTC (first period). The background grayscale shading is the Z_H field at 1 km with darker shading representing higher Z_H.

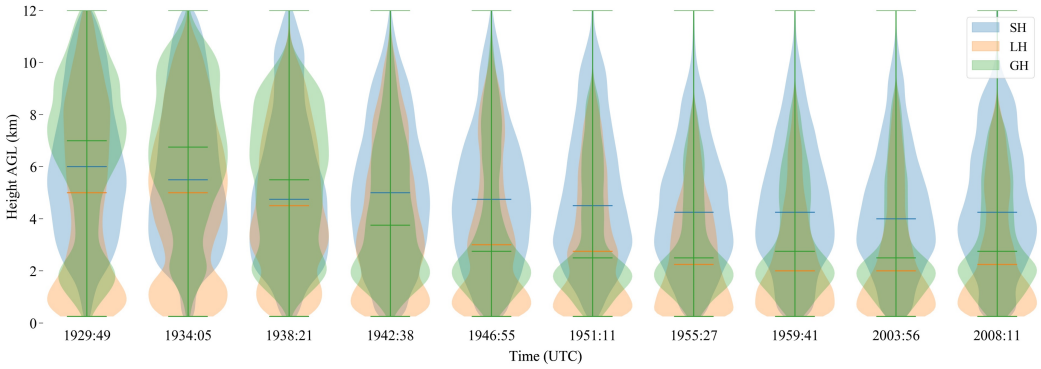

Figure 13. Height AGL distribution of SH, LH, and GH spanning the entirety of the analysis period of KTLX from 1929:49 to 2008:11 UTC. The horizontal markers within the violin plots depict the median of the respective hail class.

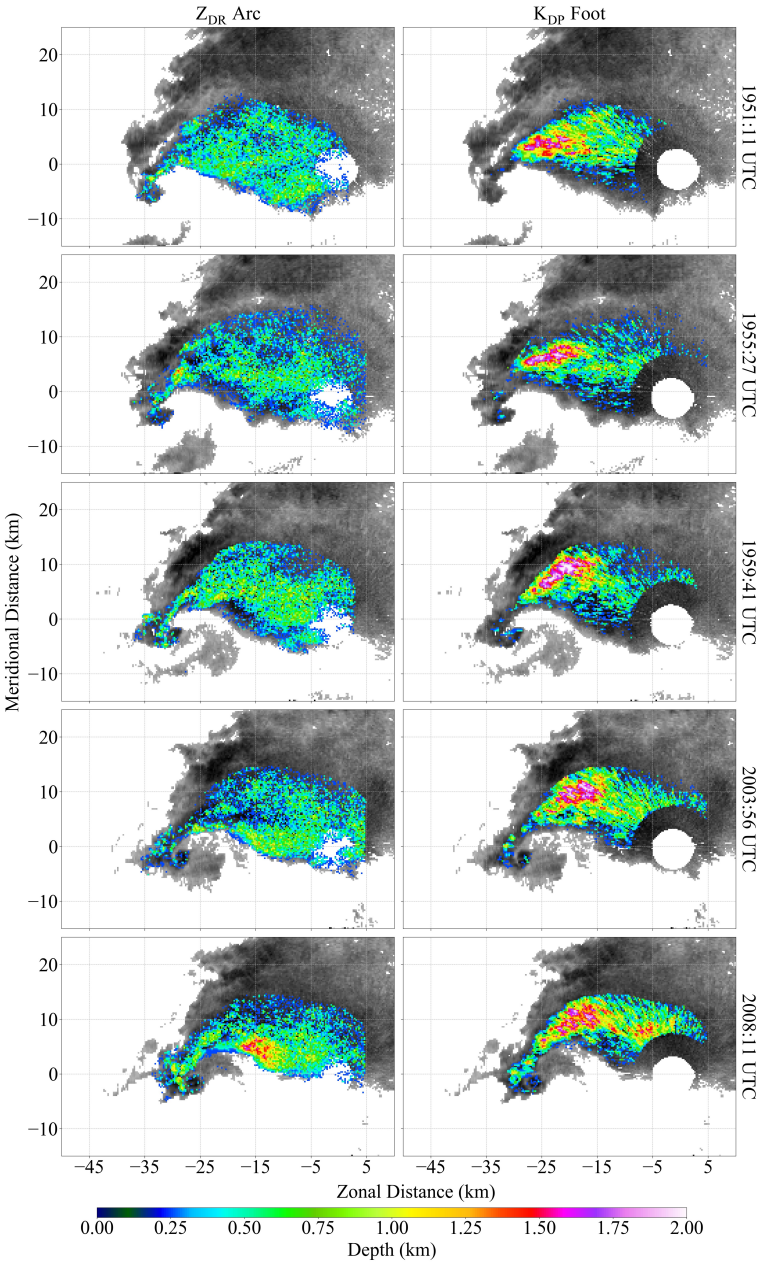

Figure 14. As in Figure 12, except for scans from 1951:11 to 2008:11 UTC (second period).

3.2.2. Z_{DR} and K_{DP} Columns

Column characteristics are known to be intrinsically related to updraft properties [39,41,44] and as such are useful signatures to analyze updraft evolution through tornadogenesis and intensification. The analysis of the Z_{DR} and K_{DP} columns relies solely on KTLX data as it is the only radar that sufficiently samples above the ambient 0 °C height (~4.2 km AGL). In the first period, there is an overall decreasing trend in Z_{DR} column volumetric extent and depth (Figure 15) as compared to trends in K_{DP} column which are more variable. The volumetric extent holds fairly steady at ~20 km^3 except at 1943 UTC when there is a sharp increase to 30 km^3; K_{DP} column depth fluctuates up and down but still shows an overall decreasing trend similar to the Z_{DR} column depth. General decreasing trends in Z_{DR} and K_{DP} column height prior to tornadogenesis are consistent with [98,99]. It has been hypothesized that as the LLM intensifies, the downward-directed perturbation pressure gradient force (PGF) towards the LLM also strengthens, resulting in a weakened updraft [18,100–102] and a subsequent decrease in the extent of the Z_{DR} and K_{DP} columns. Visually, weakening of the column in both depth and areal extent is clearly evident in both Z_{DR} and K_{DP} depth fields (Figure 16). The largest consecutive decrease in KTLX for both Z_{DR} and K_{DP} columns occurs between 1942:38 and 1946:55 UTC, which is coincident with transient increases in ΔV_r, inferred strengthening of the LLM, and increased downward-directed perturbation PGF.

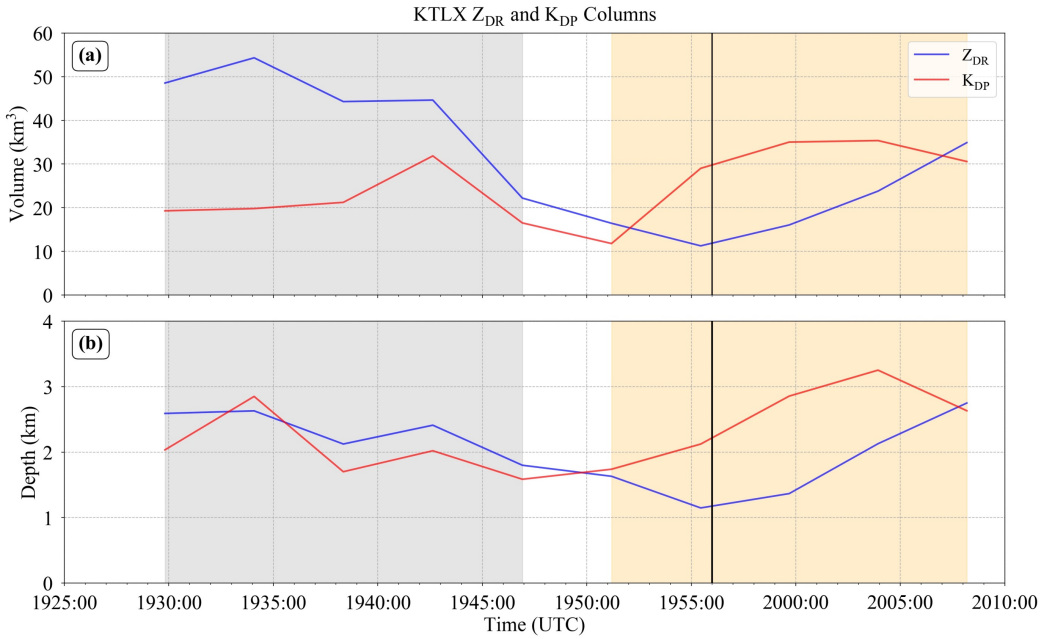

Figure 15. Using KTLX: (**a**) volumetric extent of the Z_{DR} and K_{DP} columns and (**b**) 90th percentile of the depth for both columns. The gray and orange shaded regions mark the first and second period, respectively, with the solid black vertical line denoting the time of tornadogenesis.

Whereas the decrease in Z_{DR} and K_{DP} columns' heights have been noted in [98,99] leading up to tornadogenesis, the supercell exhibits differences in the Z_{DR} and K_{DP} columns' evolution through and following tornadogenesis not previously documented. Z_{DR} and K_{DP} columns show opposing trends in behavior 5–10 min before tornadogenesis, with the K_{DP} column deepening and increasing in volumetric extent 5–10 min before the Z_{DR} column. Increases in volumetric extent occur faster for the K_{DP} column, growing from approximately 10 km^3 to 35 km^3 from 1951 to 1959 UTC. The offset timing between K_{DP} column and foot growth, the latter of which occurs earlier at 1946:55 UTC, suggests that early deepening of the K_{DP} column may result from small to medium drops concentrated just north of the updraft (depicted by the K_{DP} foot) being ingested by the updraft, which are lofted faster and higher than larger drops associated with the Z_{DR} column [39,41]. Partial

freezing of these lofted smaller drops result in mixed-phase hydrometeors, known to contribute to the production of the K_{DP} column [37]. Moreover, advection of smaller drops closer to the LLM by momentum surges that are recirculated into the updraft may be a contributing factor to K_{DP} column growth, along with influence of the echo merger around this time.

After tornadogenesis, as the updraft continues to loft smaller drops, the K_{DP} column continues to deepen over 3 km above the 0°C height until 2003:56 UTC (Figures 15 and 17). Whereas volumetric extent of the Z_{DR} column does increase slightly from 1955:27 to 1959:41 UTC, the first sign of any Z_{DR} column deepening is delayed until 1959:41 to 2003:56 UTC. Delayed deepening of the Z_{DR} column mirrors delayed post-tornadogenesis rapid intensification patterns in ΔV_r. This suggests Z_{DR} column deepening does not materialize until the intensifying updraft and associated strengthening tornado is enough to overcome the downward-directed perturbation PGF, allowing for lofting of larger drops farther above the 0 °C height. By 2008:11 UTC, volumetric extent and depth of the Z_{DR} and K_{DP} columns are nearly equal. Whereas inferences of updraft characteristics from Z_{DR} and K_{DP} columns have been previously noted, this is the first study in which the phasing of the two signatures—more specifically the delay in Z_{DR} column growth relative to K_{DP} column growth—has been documented.

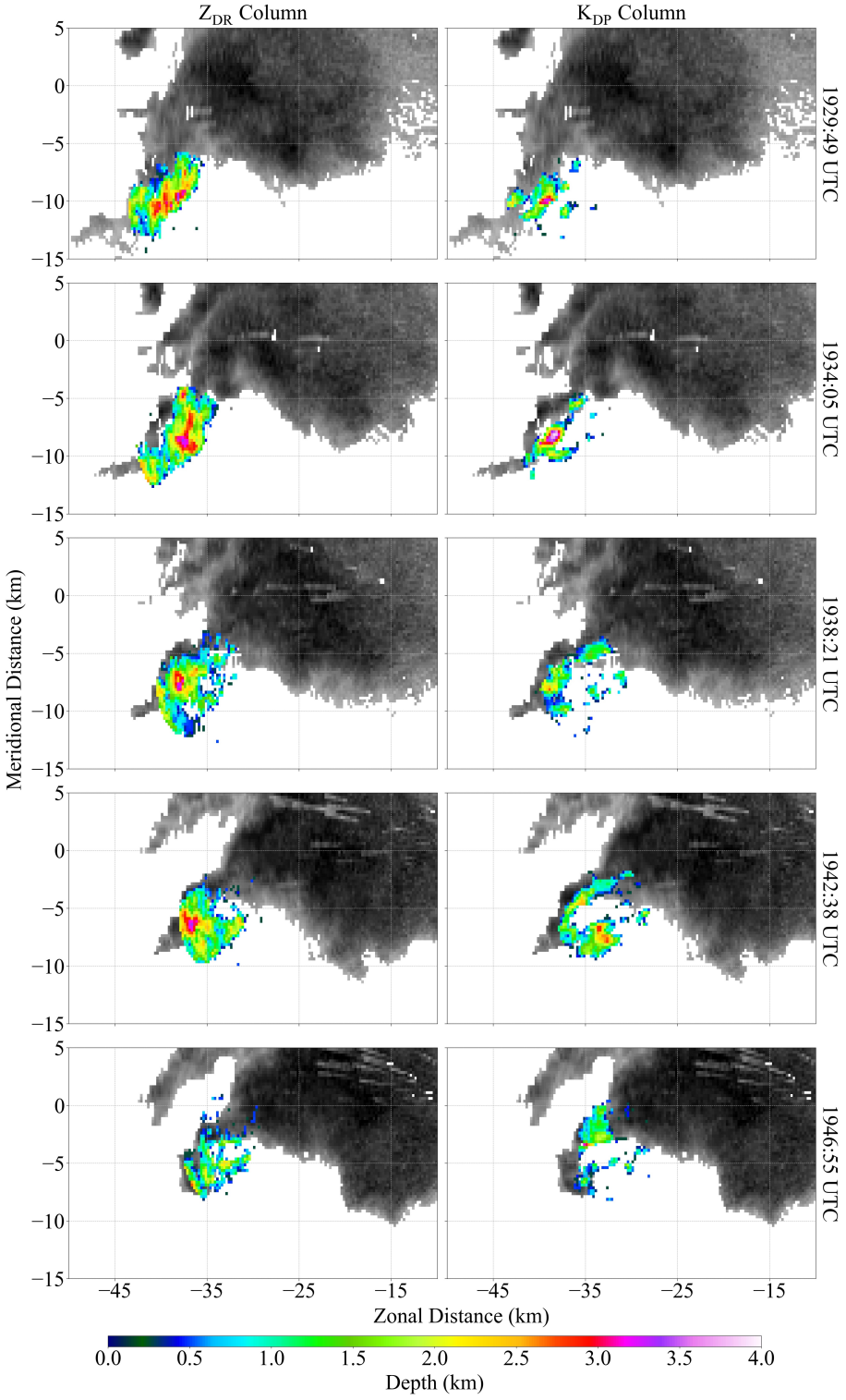

Figure 16. Plot of the depth field for Z_{DR} and K_{DP} columns from KTLX for five consecutive radar scans from 1929:49 to 1946:55 UTC (first period). The background grayscale shading is as in Figure 12.

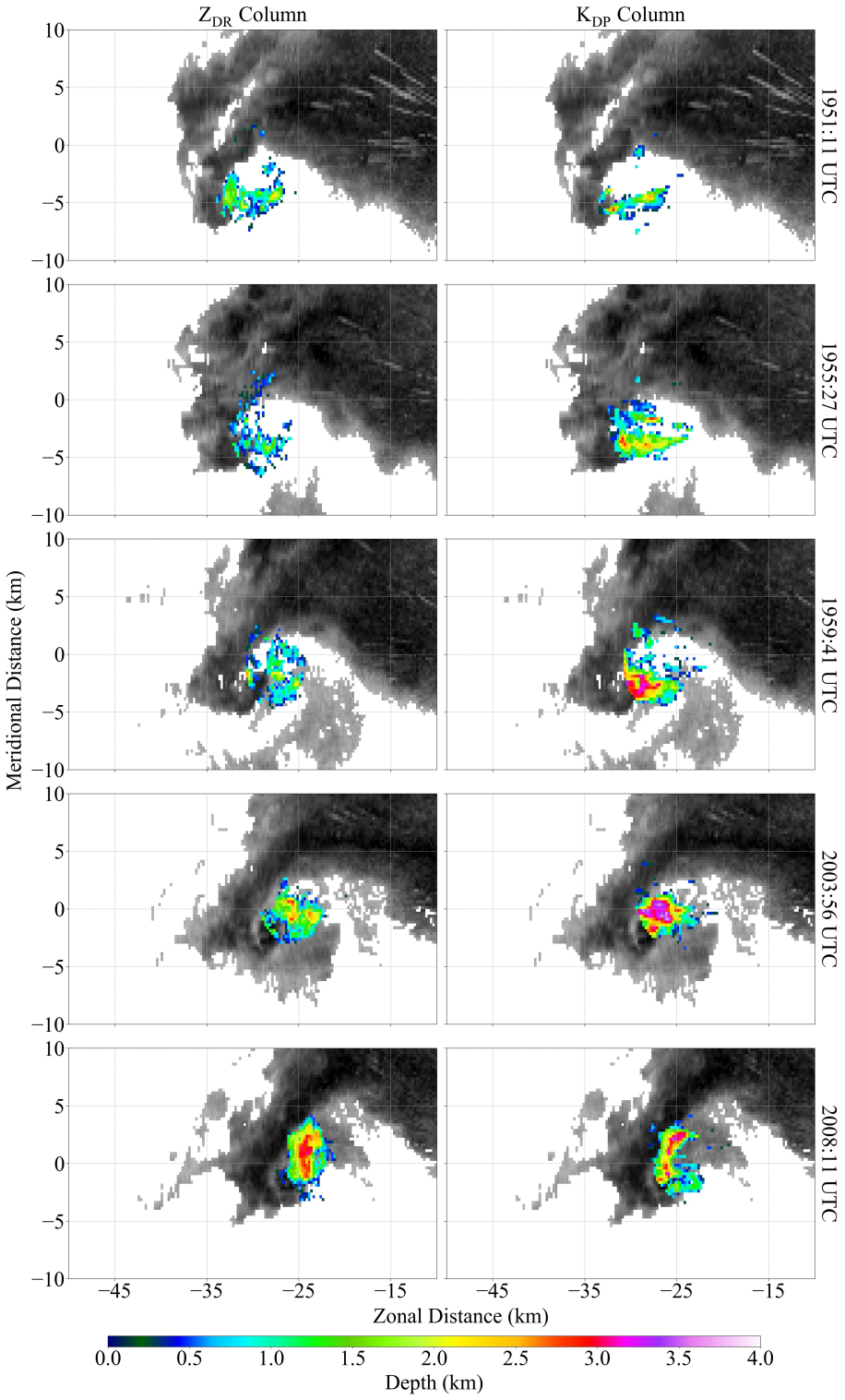

Figure 17. As in Figure 16, except from 1951:11 UTC to 2008:11 UTC (second period).

4. Conclusions

This study presents a multi-radar analysis of the 20 May 2013 Moore, Oklahoma, U.S. supercell that produced an EF5 tornado. Data came from a suite of multi-wavelength radars varying in spatial, temporal, and volumetric capabilities; whereas the PX-1000 temporally resolved 20-s PPIs, three WSR-88Ds—KTLX, KOUN, and KCRI—provided full volume coverage patterns. The suite of multi-wavelength radars allowed for an intercomparison of HCA performance between S- and X-band from [71] for S-band and [63] for X-band

with an additional modification to include size classifications of hail [72]. Though X- and S-band showed good agreement for rain and hail classes, performance can be improved in regards to BD/RA and GH/LH classes for X-band by modifying membership functions and attenuation algorithms in the future. A debris class was added for both X- and S-bands following [49]; to our knowledge, this is the first study to implement and compare TDS HCAs at X- and S-bands, opening the door for analysis on differences in debris detectability between radar wavelengths. The (T)DS class showed close agreement after tornadogenesis, suggesting successful implementation of the debris class to X-band, and have highlighted the necessity of PX-1000 in resolving characteristics of debris lofting and differences in debris detectability between the wavelengths. Debris lofting in the pre-tornadic mesocyclone are shown to be periodic and correlate with momentum surges within the hook echo. However, higher sensitivity of X-band to rain compared to S-band means T(DS) detection can suffer in low debris periods and/or higher precipitation entrainment. Because X-band has both present (non-U.S. operational radars) and future (gap-filling radars in the U.S.) uses, these comparisons of performance between wavelengths are important to tornado detection worldwide.

High-spatiotemporal resolution of PX-1000 and successful implementation of HCA to X-band provided the framework to explore the structural and microphysical progression of the hook echo during pre-tornadic momentum surges. Four transient intensifications of the LLM were evident in ΔV_r, each lasting ~1–2 min, two of which were associated with prominent momentum surges at 1952:27 and 1957:05 UTC, the latter occurring in conjunction with tornadogenesis. Structurally, the momentum surges were characterized by inbound V_r surging ahead of the LLM and advancing Z_H gradients and high pockets of Z_H cyclonically around the hook echo at 25–30 m s^{-1}; the presence of DRCs was also noted. Microphysically, surge A was marked by a decrease in Z_{DR} and ρ_{hv}, a decrease in BD, and the first detection of DS. The onset of surge B showed similar characteristics to surge A but with significantly more DS points—this is consistent with an uptick in damage indicators [55,89] and video-evidence of a debris cloud/confluent tree fall patterns, suggestive of an unconfirmed brief, weak tornado. Heavy precipitation entrainment by surge maturity, however, increased both Z_{DR} and ρ_{hv} around the LLM and led to a dominance of HR, masking any (T)DS.

Lastly, volumetric examination of Z_{DR} and K_{DP} signatures are used to infer characteristics of hail distributions, DSS, and the updraft through tornadogenesis and intensification. Although these polarimetric signatures have been used to analyze supercell characteristics/evolution (Z_{DR} more so than K_{DP}), few studies have considered the evolution of multiple signatures in conjunction with high-temporal V_r data. In the first period, leading up to tornadogenesis, the Z_{DR} arc remained relatively diffuse through 1946:55 UTC, whereas the K_{DP} foot showed more explosive growth as smaller drops concentrated downshear of the updraft within a deeper layer [29,30]. In addition, hail distributions from KTLX suggest water shedding from hail fallout, especially between 1938:21 and 1946:55 UTC, may have contributed to the maturation of the K_{DP} foot—alternatively, high concentrations of hail below 2 km may have disrupted DSS processes and resulted in diffuseness of the Z_{DR} arc [28,64,73,97]. Z_{DR} and K_{DP} columns weaken prior to tornadogenesis, which is suggestive of a weakening updraft consistent with [98,99].

After tornadogenesis at 1956 UTC, there are two periods of rapid tornadic intensification where ΔV_r increases to: (1) ~70 m s^{-1} from ~1959–2001 UTC and (2) 90 m s^{-1} from ~2003–2005 UTC. TDS quantification through PX-1000 pairs well with this analysis, showing two periods of rapid growth coincident with the ΔV_r intensifications. The K_{DP} foot remained mature through the end of the analysis period, whereas maturation of the Z_{DR} arc was significantly delayed with a concentration of larger drops through a deeper layer not occurring until 2008:11 UTC. Similarly, while the K_{DP} column showed rapid deepening just prior to and through tornadogenesis, more significant deepening of the Z_{DR} column was delayed until the end of the analysis period. Earlier onset of K_{DP} column growth may have been due to a number of factors, including earlier maturation of the K_{DP}

foot from hail fallout, influx of smaller drops into the LLM by momentum surges, and/or the influence of an echo merger. Nevertheless, this study is the first to document the offset phasing of these two signatures.

Owing to the availability of volumetric data from KTLX, KOUN, and KCRI, and the high-temporal resolution PX-1000, opportunities for further analyses are abundant. Study of the detectability of TDSs at X-band and improving TDS HCA membership functions will be useful for the evaluation of current and future radar networks (e.g., gap-filling radar applications) for tornadoes. Based on our findings, additional research is needed to evaluate if X-band radars would have more difficulty in detecting TDSs than S-band radars. Extending the ΔV_r, microphysical, and Z_{DR}/K_{DP} analyses into the mature, failed occlusion, and dissipation stages of the tornadic supercell, as well as application to other cases, is left for future work. Lastly, investigation into the thermodynamic and kinematic properties of the east-west oriented boundary and its role in tornadogenesis and maintenance should be conducted.

Author Contributions: Conceptualization, C.N.S., D.J.B. and R.D.P.; methodology, C.N.S. and D.J.B.; software, C.N.S.; validation, C.N.S.; formal analysis, C.N.S.; investigation, C.N.S. and C.M.K.; resources, C.N.S.; data curation, C.N.S.; writing—original draft preparation, C.N.S.; writing—review and editing, C.N.S., D.J.B., R.D.P. and C.M.K.; visualization, C.N.S.; supervision, D.J.B. and R.D.P.; project administration, D.J.B. and R.D.P.; funding acquisition, D.J.B. and R.D.P. All authors have read and agreed to the published version of the manuscript.

Funding: Funding for this research and first author's assistantship was provided by Nanowave Technologies Inc and NSF grant AGS-1823478.

Institutional Review Board Statement: Not applicable.

Informed Consent Statement: Not applicable.

Data Availability Statement: The PX-1000 data presented in this study are available at https://arrc.ou.edu/data.html, accessed on 20 February 2021, and KOUN and KCRI data through C.M.K. KTLX data are publicly available and can be accessed via https://s3.amazonaws.com/noaa-nexrad-level2/index.html, accessed on 20 February 2021, though stored moment data can also be provided if requested.

Acknowledgments: The authors thank Pierre Kirstetter who served on the first author's M.S. committee and provided valuable input towards the improvement of this research. We also thank Casey Griffin for his invaluable contributions, including the instruction of Solo II, and Boonleng Cheong and Jim Kurdzo for operating PX-1000 on 20 May 2013 as well as providing post-processed PX-1000 data. Lastly, the authors are appreciative of the feedback received from three anonymous reviewers and the editor which contributed to the betterment of this manuscript.

Conflicts of Interest: The authors declare no conflict of interest. The funding sponsors had no role in the design of the study; in the collection, analyses, or interpretation of data; in the writing of the manuscript, or in the decision to publish the results.

References

1. Isom, B.; Palmer, R.; Kelley, R.; Meier, J.; Bodine, D.; Yeary, M.; Cheong, B.L.; Zhang, Y.; Yu, T.Y.; Biggerstaff, M.I. The Atmospheric Imaging Radar: Simultaneous volumetric observations using a Phased Array Weather Radar. *J. Atmos. Ocean. Technol.* **2013**, *30*, 655–675. [CrossRef]
2. Pazmany, A.L.; Mead, J.B.; Bluestein, H.B.; Snyder, J.C.; Houser, J.B. A mobile rapid-scanning X-band polarimetric (RaXPol) Doppler radar system. *J. Atmos. Ocean. Technol.* **2013**, *30*, 1398–1413. [CrossRef]
3. Kurdzo, J.M.; Nai, F.; Bodine, D.J.; Bonin, T.A.; Palmer, R.D.; Cheong, B.L.; Lujan, J.; Mahre, A.; Byrd, A.D. Observations of severe local storms and tornadoes with the Atmospheric Imaging Radar. *Bull. Am. Meteorol. Soc.* **2017**, *98*, 915–935. [CrossRef]
4. Weber, M.E.; Cho, J.Y.N.; Herd, J.S.; Flavin, J.M.; Benner, W.E.; Torok, G.S. The next-generation multimission U.S. surveillance radar network. *Bull. Am. Meteorol. Soc.* **2007**, *88*, 1739–1751. [CrossRef]
5. Zrnic, D.S.; Kimpel, J.F.; Forsyth, D.E.; Shapiro, A.; Crain, G.; Ferek, R.; Heimmer, J.; Benner, W.; McNellis, F.T.J.; Vogt, R.J. Agile-beam phased array radar for weather observations. *Bull. Am. Meteorol. Soc.* **2007**, *88*, 1753–1766. [CrossRef]
6. Yoshikawa, E.; Ushio, T.; Kawasaki, Z.; Yoshida, S.; Morimoto, T.; Mizutani, F.; Wada, W. MMSE beam forming on fast-scanning phased array weather radar. *IEEE Trans. Geosci. Remote Sens.* **2012**, *51*, 3077–3088. [CrossRef]

7. Bluestein, H.B.; Rauber, R.M.; Burgess, D.W.; Albrecht, B.; Ellis, S.M.; Richardson, Y.P.; Jorgensen, D.P.; Frasier, S.; Chilson, P.; Palmer, R.D.; et al. Radar in atmospheric sciences and related research: Current systems, emerging technology, and future needs. *Bull. Am. Meteorol. Soc.* **2014**, *95*, 1850–1861. [CrossRef]
8. Markowski, P.M. Hook echoes and rear-flank downdrafts: A review. *Mon. Weather Rev.* **2002**, *130*, 852–876. [CrossRef]
9. Grzych, M.L.; Lee, B.D.; Finley, C.A. Thermodynamic analysis of supercell rear-flank downdrafts from Project ANSWERS. *Mon. Weather Rev.* **2007**, *135*, 240–246. [CrossRef]
10. Hirth, B.D.; Schroeder, J.L.; Weiss, C.C. Surface analysis of the rear-flank downdraft outflow in two tornadic supercells. *Mon. Weather Rev.* **2008**, *136*, 2344–2363. [CrossRef]
11. Lee, B.D.; Finley, C.A.; Karstens, C.D. The Bowdle, South Dakota, cyclic tornadic supercell of 22 May 2010: Surface analysis of rear-flank downdraft evolution and multiple internal surges. *Mon. Weather Rev.* **2012**, *140*, 3419–3441. [CrossRef]
12. Atkins, N.T.; Butler, K.M.; Flynn, K.R.; Wakimoto, R.M. An integrated damage, visual, and radar analysis of the 2013 Moore, Oklahoma EF5 tornado. *Bull. Am. Meteorol. Soc.* **2014**, *95*, 1549–1561. [CrossRef]
13. Skinner, P.S.; Weiss, C.C.; French, M.M.; Bluestein, H.B.; Markowski, P.M.; Richardson, Y.P. VORTEX2 observations of a low-level mesocyclone with multiple internal rear-flank downdraft momentum surges in the 18 May 2010 Dumas, Texas, supercell. *Mon. Weather Rev.* **2014**, *142*, 2935–2960. [CrossRef]
14. Adlerman, E.J. Numerical Simulations of Cyclic Storm Behavior: Mesocylogenesis and Tornadogenesis. Ph.D. Thesis, University of Oklahoma, Norman, OK, USA, 2003.
15. Mashiko, W.; Niino, H.; Kato, T. Numerical simulation of tornadogenesis in an outer-rainband minisupercell of Typhoon ShanShan on 17 September 2006. *Mon. Weather Rev.* **2009**, *137*, 4238–4260. [CrossRef]
16. Schenkman, A.D.; Xue, M.; Hu, M. Tornadogenesis in a high-resolution simulation of the 8 May 2003 Oklahoma City supercell. *J. Atmos. Sci.* **2014**, *71*, 130–154. [CrossRef]
17. Dahl, J.M.L.; Parker, M.D.; Wicker, L.J. Imported and storm-generated near-ground vertical vorticity in a simulated supercell. *J. Atmos. Sci.* **2014**, *71*, 3027–3051. [CrossRef]
18. Adlerman, E.J.; Droegemeier, K.K.; Davies-Jones, R. A numerical simulation of cyclic mesocyclogenesis. *J. Atmos. Sci.* **1999**, *56*, 2045–2069. [CrossRef]
19. Finley, C.A.; Lee, B.D. High-resolution mobile mesonet observations of RFD surges in the June 9 Basset, Nebraska supercell during Project ANSWERS 2003. In Proceedings of the 22nd Conference on Severe Local Storms, Hyannis, MA, USA, 7 October 2004.
20. Adlerman, E.J.; Droegemeier, K.K. The dependence of numerically simulated cyclic mesocyclogenesis upon environmental vertical wind shear. *Mon. Weather Rev.* **2005**, *133*, 3595–3623. [CrossRef]
21. Kumjian, M.R.; Ryzhkov, A.V. Polarimetric signatures in supercell thunderstorms. *J. Appl. Meteorol. Climatol.* **2008**, *48*, 1940–1961. [CrossRef]
22. Van Den Broeke, M.S.; Straka, J.M.; Rasmussen, E.N. Polarimetric radar observations at low levels during tornado life cycles in a small sample of classic southern Plains supercells. *J. Appl. Meteorol. Climatol.* **2008**, *47*, 1232–1247. [CrossRef]
23. Van Den Broeke, M.S. Polarimetric radar metrics related to tornado life cycles and intensity in supercell storms. *Mon. Weather Rev.* **2017**, *145*, 3671–3686. [CrossRef]
24. Van Den Broeke, M.S. Disdrometer, polarimetric radar, and condensation nuclei observations of supercell and multicell storms on 11 June 2018 in eastern Nebraska. *Atmosphere* **2020**, *11*, 770. [CrossRef]
25. Kumjian, M.R.; Picca, J.C.; Ganson, S.M.; Ryzhkov, A.V.; Krause, J. Polarimetric radar characteristics of large hail. In Proceedings of the 25th Conference on Severe Local Storms, Denver, CO, USA, 13 October 2010.
26. Dawson, D.T.; Mansell, E.R.; Jung, Y.; Wicker, L.J.; Kumjian, M.R.; Xue, M. Low-level ZDR Signatures in Supercell Forward Flanks: The role of size sorting and melting of hail. *J. Atmos. Sci.* **2014**, *71*, 276–299. [CrossRef]
27. Romine, G.S.; Burgess, D.W.; Wilhelmson, R.B. A dual-polarization-radar-based assessment of the 8 May 2003 Oklahoma City tornado supercell. *Mon. Weather Rev.* **2008**, *136*, 2849–2870. [CrossRef]
28. Palmer, R.D.; Bodine, D.; Kumjian, M.; Cheong, B.; Zhang, G.; Cao, Q.; Bluestein, H.B.; Ryzhkov, A.; Yu, T.Y.; Wang, Y. The 10 May 2010 tornado outbreak in central Oklahoma: Potential for new science with high-resolution polarimetric radar. *Bull. Am. Meteorol. Soc.* **2011**, *92*, 871–891. [CrossRef]
29. Crowe, C.C.; Schultz, C.J.; Kumjian, M.; Carey, L.D.; Petersen, W.A. Use of dual-polarization signatures in diagnosing tornado potential. *Electron. J. Oper. Meteorol.* **2012**, *13*, 57–78.
30. Loeffler, S.D.; Kumjian, M.R. Quantifying the separation of enhanced Z_{DR} and K_{DP} regions in nonsupercell tornadic storms. *Weather Forecast.* **2018**, *33*, 1143–1157. [CrossRef]
31. Loeffler, S.D.; Kumjian, M.R.; Jurewicz, M.; French, M.M. Differentiating between tornadic and nontornadic supercells using polarimetric radar signatures of hydrometeor size sorting. *Geophys. Res. Lett.* **2020**, *47*, e2020GL088242. [CrossRef]
32. Hall, M.M.; Cherry, S.M.; Goddard, J.F. Identification of hydrometeors and other targets by dual-polarization radar. *Radio Sci.* **1984**, *19*, 132–140. [CrossRef]
33. Illingworth, A.J.; Caylor, I.J. Identification of precipitation using dual-polarization radar. In Proceedings of the Tenth International Cloud Physics Conference, Bad Homburg, Germany, 15–20 August 1988; pp. 372–377. Available online: https://apps.dtic.mil/sti/citations/ADA196726 (accessed on 20 February 2021).

34. Conway, J.W.; Zrnić, D.S. A study of embryo production and hail growth using dual-Doppler and multiparameter radars. *Mon. Weather Rev.* **1993**, *121*, 2511–2528. [CrossRef]
35. Brandes, E.A.; Vivekanandan, J.; Tuttle, J.D.; Kessinger, C.J. A study of thunderstorm microphysics with multiparameter radar and aircraft observations. *Mon. Weather Rev.* **1995**, *123*, 3129–3143. [CrossRef]
36. Zrnić, D.S.; Ryzhkov, A.V. Polarimetry for weather surveillance radars. *Bull. Am. Meteorol. Soc.* **1999**, *80*, 389–406. [CrossRef]
37. Loney, M.L.; Zrnić, D.S.; Straka, J.M.; Ryzhkov, A.V. Enhanced polarimetric radar signatures above the melting level in a supercell storm. *J. Appl. Meteorol.* **2002**, *41*, 1179–1194. [CrossRef]
38. Kumjian, M.; Ryzhkov, A.V.; Melnikov, V.M.; Schuur, T.J. Rapid-scan super-resolution observations of a cyclic supercell with a dual-polarization WSR-88D. *Mon. Weather Rev.* **2010**, *138*, 3762–3786. [CrossRef]
39. Kumjian, M.R.; Khain, A.P.; Benmoshe, N.; Ilotoviz, E.; Ryzhkov, A.V.; Phillips, V.T.J. The anatomy and physics of Z_{DR} columns: Investigating a polarimetric radar signature with a spectral bin microphysical model. *J. Appl. Meteorol. Climatol.* **2014**, *53*, 1820–1843. [CrossRef]
40. Homeyer, C.R.; Kumjian, M.R. Microphysical characteristics of overshooting convection from polarimetric radar observations. *J. Atmos. Sci.* **2015**, *72*, 870–891. [CrossRef]
41. Snyder, J.C.; Bluestein, H.B.; Dawson, D.T., II; Jung, Y. Simulations of polarimetric, X-band radar signatures in supercells. Part II: Z_{DR} columns and rings and K_{DP} columns. *J. Appl. Meteorol. Climatol.* **2017**, *56*, 2001–2026. [CrossRef]
42. Hubbert, J.; Bringi, V.N.; Carey, L.D. CSU-CHILL polarimetric measurements from a severe hailstorm in eastern Colorado. *J. Appl. Meteorol.* **1998**, *37*, 749–755. [CrossRef]
43. Snyder, J.C.; Bluestein, H.B.; Venkatesh, V.; Frasier, S.J. Observations of polarimetric signatures in supercells by an X-band mobile Doppler radar. *Mon. Weather Rev.* **2013**, *141*, 3–29. [CrossRef]
44. Snyder, J.C.; Kumjian, M.R.; Khain, A.P.; Picca, J. A Z_{DR} Column detection algorithm to examine convective storm updrafts. *Weather Forecast.* **2015**, *30*, 1819–1844. [CrossRef]
45. Ryzhkov, A.V.; Schuur, T.J.; Burgess, D.W.; Zrnić, D.S. Polarimetric tornado detection. *J. Appl. Meteorol.* **2005**, *44*, 557–570. [CrossRef]
46. Bluestein, H.B.; French, M.M.; Tanamachi, R.L.; Frasier, S.; Hardwick, K.; Junyent, F.; Pazmany, A. Close-range observations of tornadoes in supercells made with a dual-polarization, X-band, mobile Doppler radar. *Mon. Weather Rev.* **2007**, *135*, 1522–1543. [CrossRef]
47. Bodine, D.; Kumjian, M.R.; Palmer, R.D.; Heinselman, P.L.; Ryzhkov, A.V. Tornado damage estimation using polarimetric radar. *Weather Forecast.* **2013**, *28*, 139–158. [CrossRef]
48. Bodine, D.J.; Palmer, R.D.; Zhang, G. Dual-wavelength polarimetric radar analyses of tornadic debris signatures. *J. Appl. Meteorol. Climatol.* **2014**, *53*, 242–261. [CrossRef]
49. Snyder, J.C.; Ryzhkov, A.V. Automated detection of polarimetric tornadic debris signatures using a hydrometeor classification algorithm. *J. Appl. Meteorol. Climatol.* **2015**, *54*, 1861–1870. [CrossRef]
50. Cheong, B.L.; Bodine, D.J.; Fulton, C.J.; Torres, S.M.; Maruyama, T.; Palmer, R.D. SimRadar: A polarimetric radar time-series simulator for tornadic debris studies. *IEEE Trans. Geosci. Remote Sens.* **2017**, *55*, 2858–2870. [CrossRef]
51. Van Den Broeke, M.S.; Jauernic, S.T. Spatial and Temporal Characteristics of Polarimetric Tornadic Debris Signatures. *J. Appl. Meteorol. Climatol.* **2014**, *53*, 2217–2231. [CrossRef]
52. Saari, M.D.W.; Lawton, R.M.; Schultz, C.J.; Carey, L.D. Early characteristics of the polarimetric tornadic debris signature associated with the 20 May 2013 Newcastle-Moore, Oklahoma, tornado. *J. Oper. Meteorol.* **2014**, *2*, 110–114. [CrossRef]
53. Broeke, M.S.V.D.; Broeke, C.A.V.D. Polarimetric radar observations from a waterspout-producing thunderstorm. *Weather Forecast.* **2015**, *30*, 329–348. [CrossRef]
54. Broeke, M.S.V.D. Potential tornado warning improvement resulting from utilization of the TDS in the warning decision process. *J. Oper. Meteorol.* **2017**, *5*, 121–133. [CrossRef]
55. Ortega, K.; Burgess, D.; Garfield, G.; Karstens, C.; LaDue, J.; Marshall, T.; Meyer, T.; Smith, B.; Smith, R.; Spegeher, D.; et al. Damage survey and analysis of the 20 May 2013 Newcastle-Moore EF-5 tornado. In *Special Sym. on Severe Local Storms: The Current State of the Science and Understanding Impacts*; American Meteorological Society: Atlanta, GA, USA, 2014.
56. Kurdzo, J.M.; Bodine, D.J.; Cheong, B.L.; Palmer, R.D. High-temporal resolution polarimetric X-band Doppler radar observations of the 20 May 2013 Moore, Oklahoma tornado. *Mon. Weather Rev.* **2015**, *143*, 2711–2735. [CrossRef]
57. Satrio, C.N. Multi-Radar Analysis of the 20 May 2013 Moore, Oklahoma Supercell through Tornadogenesis and Intensification. Ph.D. Thesis, University of Oklahoma, Norman, OK, USA, 2019.
58. Burgess, D.; Ortega, K.; Stumpf, G.; Garfield, G.; Karstens, C.; Meyer, T.; Smith, B.; Speheger, D.; Ladue, J.; Smith, R.; et al. 20 May 2013 Moore, Oklahoma tornado: Damage survey and analysis. *Weather Forecast.* **2014**, *29*, 1229–1237. [CrossRef]
59. Kurdzo, J.M.; Cheong, B.L.; Palmer, R.D.; Zhang, G.; Meier, J.B. A pulse compression waveform for improved-sensitivity weather radar observations. *J. Atmos. Ocean. Technol.* **2014**, *31*, 2713–2731. [CrossRef]
60. Cheong, B.L.; Kelley, R.; Palmer, R.D.; Zhang, Y.; Yeary, M.; Yu, T.Y. PX-1000: A solid-state polarimetric X-band weather radar and time–frequency multiplexed waveform for blind range mitigation. *IEEE Trans. Instr. Meas.* **2013**, *62*, 3064–3072. [CrossRef]
61. Lei, L.; Zhang, G.; Doviak, R.J.; Palmer, R.; Cheong, B.L.; Xue, M.; Cao, Q.; Li, Y. Multilag correlation estimators for polarimetric radar measurements in the presence of noise. *J. Atmos. Ocean. Technol.* **2012**, *29*, 772–795. [CrossRef]

62. Bringi, V.N.; Chandrasekar, V.; Balakrishnan, N.; Zrnić, D.S. An examination of propagation effects in rainfall at microwave frequencies. *J. Atmos. Ocean. Technol.* **1990**, *7*, 829–840. [CrossRef]
63. Snyder, J.C.; Bluestein, H.B.; Zhang, G.; Frasier, S.J. Attenuation correction and hydrometeor classification of high-resolution, X-band, dual-polarized mobile radar measurements in severe convective storms. *J. Atmos. Ocean. Technol.* **2010**, *27*, 1979–2001. [CrossRef]
64. Picca, J.C.; Ryzhkov, A.V. A dual-wavelength polarimetric analysis of the 16 May 2010 Oklahoma City extreme hailstorm. *Mon. Weather Rev.* **2012**, *140*, 1385–1403. [CrossRef]
65. Wilson, M.B.; Broeke, M.S.V.D. An Automated Python Algorithm to Quantify Z_{DR} Arc and K_{DP}-Z_{DR} Separation Signatures in Supercells. *J. Atmos. Ocean. Technol.* **2020**, *38*, 371–386. [CrossRef]
66. Weaver, H.J. *Applications of Discrete and Continuous Fourier Analysis*; J. Wiley and Sons: Hoboken, NJ, USA, 1983; p. 582.
67. Trapp, R.J.; Doswell, C.A. Radar data objective analysis. *J. Atmos. Ocean. Technol.* **2000**, *17*, 105–120. [CrossRef]
68. Cressman, G.P. An operational objective analysis system. *Mon. Weather Rev.* **1959**, *87*, 367–374. [CrossRef]
69. Barnes, S.L. A technique for maximizing details in numerical weather map analysis. *J. Appl. Meteorol.* **1964**, *3*, 396–409. [CrossRef]
70. Schuur, T.J.; Ryzhkov, A.V.; Heinselman, P.L. *Observations and Classification of Echoes with the Polarimetric WSR-88D Radar*; Technical Repor; NOAA/National Severe Storms Laboratory: Norman, OK, USA, 2003.
71. Park, H.S.; Ryzhkov, A.V.; Zrnić, D.S.; Kim, K. The hydrometeor classification algorithm for the polarimetric WSR-88D: Description and application to an MCS. *Weather Forecast.* **2009**, *24*, 730–748. [CrossRef]
72. Ryzhkov, A.V.; Kumjian, M.R.; Ganson, S.M.; Zhang, P. Polarimetric radar characteristics of melting hail. Part II: Practical implications. *J. Appl. Meteorol. Climatol.* **2013**, *52*, 2871–2886. [CrossRef]
73. Kumjian, M.R.; Ryzhkov, A.V. Storm-relative helicity revealed from polarimetric radar measurements. *J. Atmos. Sci.* **2009**, *66*, 667–685. [CrossRef]
74. Van Den Broeke, M.S. Polarimetric Variability of classic supercell storms as a function of environment. *J. Appl. Meteorol. Climatol.* **2016**, *55*, 1907–1925. [CrossRef]
75. Markowski, P.M.; Rasmussen, E.N.; Straka, J.M. The occurence of tornadoes in supercells interacting with boundaries during VORTEX-95. *Weather Forecast.* **1998**, *13*, 852–859. [CrossRef]
76. Rasmussen, E.N.; Richardson, S.; Straka, J.M.; Markowski, P.M.; Blanchard, D.O. The association of significant tornadoes with a baroclinic boundary on 2 June 1995. *Mon. Weather Rev.* **2000**, *128*, 174–191. [CrossRef]
77. Houston, A.L.; Wilhelmson, R.B. Observational analysis of the 27 May 1997 central Texas tornadic event. Part II: Tornadoes. *Mon. Weather Rev.* **2007**, *135*, 727–735. [CrossRef]
78. Honda, T.; Kawano, T. A possible mechanism of tornadogenesis associated with the interaction between a supercell and an outflow boundary without horizontal shear. *J. Atmos. Sci.* **2016**, *73*, 1273–1292. [CrossRef]
79. Marquis, J.; Richardson, Y.; Markowski, P.; Dowell, D.; Wurman, J. Tornado maintenance investigated with high-resolution dual-Doppler and EnKF analysis. *Mon. Weather Rev.* **2012**, *140*, 3–27. [CrossRef]
80. Kosiba, K.A.; Wurman, J.; Richardson, Y.; Markowski, P.; Robinson, P.; Marquis, J. Genesis of the Goshen County, Wyoming, tornado on 5 June 2009 during VORTEX2. *Mon. Weather Rev.* **2013**, *141*, 1157–1181. [CrossRef]
81. French, M.M.; Bluestein, H.B.; PopStefanija, I.; Baldi, C.A.; Bluth, R.T. Reexamining the Vertical Development of Tornadic Vortex Signatures in Supercells. *Mon. Weather Rev.* **2013**, *141*, 4576–4601. [CrossRef]
82. Griffin, C.B.; Bodine, D.J.; Kurdzo, J.M.; Mahre, A.; Palmer, R.D. High-temporal resolution observations of the 27 May 2015 Canadian, Texas, tornado using the Atmospheric Imaging Radar. *Mon. Weather Rev.* **2019**, *147*, 873–891. [CrossRef]
83. Mahre, A.; Kurdzo, J.M.; Bodine, D.J.; Griffin, C.B.; Palmer, R.D.; Yu, T. Analysis of the 16 May 2015 Tipton, Oklahoma, EF-3 Tornado at High Spatiotemporal Resolution Using the Atmospheric Imaging Radar. *Mon. Weather Rev.* **2018**, *146*, 2103–2124. [CrossRef]
84. Huuskonen, A.; Saltikoff, E.; Holleman, I. The operational weather radar network in Europe. *Bull. Am. Meteorol. Soc.* **2014**, *95*, 897–907. [CrossRef]
85. McLaughlin, D.; Pepyne, D.; Chandrasekar, V.; Philips, B.; Kurose, J.; Zink, M.; Droegemeier, K.; Cruz-Pol, S.; Junyent, F.; Brotzge, J.; et al. Short-wavelength technology and the potential for distributed networks of small radar systems. *Bull. Am. Meteorol. Soc.* **2009**, *90*, 1797–1818. [CrossRef]
86. Bodine, D.J.; Palmer, R.D.; Maruyama, T.; Fulton, C.J.; Zhu, Y.; Cheong, B.L. Simulated Frequency Dependence of Radar Observations of Tornadoes. *J. Atmos. Ocean. Technol.* **2016**, *33*, 1825–1842. [CrossRef]
87. Davies-Jones, R. Can a descending rain curtain in a supercell instigate tornadogenesis barotropically? *J. Atmos. Sci.* **2008**, *65*, 2469–2497. [CrossRef]
88. Kumjian, M. Precipitation properties of supercell hook echoes. *E J. Sev. Storms Meteorol.* **2011**, *6*, 1–21.
89. Karstens, C.D.; Gallus, W.A., Jr.; Lee, B.D.; Finley, C.A. Analysis of tornado-induced tree fall using aerial photography from the Joplin, Missouri, and Tuscaloosa–Birmingham, Alabama, tornadoes of 2011. *J. Appl. Meteorol. Climatol.* **2013**, *52*, 1049–1068. [CrossRef]
90. Straka, J.M.; Rasmussen, E.N.; Davies-Jones, R.P.; Markowski, P.M. An observational and idealized numerical examination of low-level counter-rotating vortices towards the rear flank of supercells. *E J. Sev. Storms Meteorol.* **2007**, *2*, 1–22.
91. Markowski, P.M.; Straka, J.M.; Rasmussen, E.N.; Davies-Jones, R.P.; Richardson, Y.; Trapp, J. Vortex lines within low-level mesocyclones obtrained from psuedo-dual-Doppler radar observations. *Mon. Weather Rev.* **2008**, *136*, 3513–3535. [CrossRef]

92. Markowski, P.M.; Richardson, Y.P. The influence of environmental low-level shear and cold pools on tornadogenesis: Insights from toy simulations. *J. Atmos. Sci.* **2014**, *71*, 243–275. [CrossRef]
93. Coffer, B.E.; Parker, M.D.; Dahl, J.M.L.; Wicker, L.J.; Clark, A.J. Volatility of tornadogenesis: An ensemble of simulated nontornadic and tornadic supercells in VORTEX2 environments. *Mon. Weather Rev.* **2017**, *145*, 4605–4625. [CrossRef]
94. Orf, L.; Wilhelmson, R.; Lee, B.; Finley, C.; Houston, A. Evolution of a long-track violent tornado within a simulated supercell. *Bull. Am. Meteorol. Soc.* **2017**, *98*, 45–68. [CrossRef]
95. Yokota, S.; Niino, H.; Seko, H.; Kunii, M.; Yamauchi, H. Important factors for tornadogenesis as revealed by high-resolution ensemble forecasts of the Tsukuba supercell tornado of 6 May 2012 in Japan. *Mon. Weather Rev.* **2018**, *146*, 1109–1132. [CrossRef]
96. Martinaitis, S.M. Radar observations of tornado-warned convection associated with tropical cyclones over Florida. *Weather Forecast.* **2017**, *32*, 165–186. [CrossRef]
97. Tanamachi, R.L.; Heinselman, P.L. Rapid-scan, polarimetric observations of central Oklahoma severe storms on 31 May 2013. *Weather Forecast.* **2016**, *31*, 19–42. [CrossRef]
98. Picca, J.C.; Snyder, J.C.; Ryzhkov, A.V. An observational analysis of Z_{DR} column trends in tornadic supercells. In Proceedings of the 37th Conference on Radar Meteorology, Norman, OK, USA, 15 September 2015.
99. Dalman, D.M.; Tanamachi, R.L.; Saunders, P.E.; Cheong, B.L.; Bodine, D.; Bluestein, H.B.; Weinhoff, Z.B. Cataloging rapid-scan observations of Z_{DR} columns in supercells. In Proceedings of the 29th Conference on Severe Local Storms, Stowe, VT, USA, 23 October 2018.
100. Brandes, E.A. Mesocyclone evolution and tornadogenesis: Some observations. *Mon. Weather Rev.* **1978**, *106*, 995–1011. [CrossRef]
101. Lemon, L.R.; Doswell, C.A. Severe Thunderstorm Evolution and Mesocyclone Structure as Related to Tornadogenesis. *Mon. Weather Rev.* **1979**, *107*, 1184–1197. [CrossRef]
102. Trapp, R.J.; Mitchell, E.D.; Tipton, G.A.; Effertz, D.W.; Watson, A.I.; Andra, D.L.; Magsig, M.A. Descending and nondescending tornadic vortex signatures detected by WSR-88Ds. *Weather Forecast.* **1999**, *14*, 625–639. [CrossRef]